Eur. Phys. J. C 45, 493–511 (2006)
Digital Object Identifier (DOI) 10.1140/epjc/s2005-02408-5

THE EUROPEAN PHYSICAL JOURNAL C

Tachyonic cyclotron radiation

R. Tomaschitz[a]

Department of Physics, Hiroshima University, 1-3-1 Kagami-yama, Higashi-Hiroshima 739-8526, Japan

Received: 2 August 2005 /
Published online: 24 November 2005 –

Abstract. We study superluminal cyclotron emission by electrons and muons in semiclassical orbits. The tachyonic line spectra of hydrogenic ions such as H, $^{56}Fe^{25+}$, and $^{238}U^{91+}$, as well as their muonic counterparts $p\mu^-$, $^{56}Fe^{26+}\mu^-$ and $^{238}U^{92+}\mu^-$ are calculated, in particular the tachyonic power transversally and longitudinally radiated, the total intensity, and the power radiated in the individual harmonics. We also investigate tachyonic continuum radiation from electrons and protons cycling in the surface and light cylinder fields of γ-ray and millisecond pulsars, such as the Crab pulsar, PSR B1509–58, and PSR J0218+4232. The superluminal spectral densities generated by non-relativistic, mildly relativistic and ultra-relativistic source particles are derived. We study the parameters determining the global shape of the transversal and longitudinal densities and the energy scales of the broadband spectrum. The observed cutoff frequency in the γ-ray band of the pulsars is used to infer the upper edge of the orbital energy, and we conclude that electrons and nuclei cycling in the surface fields can reach energies beyond the "ankle" of the cosmic ray spectrum. This suggests γ-ray pulsars as sources of ultra-high energy cosmic rays.

PACS. 41.60.Ap, 11.10.Lm, 36.10.Dr, 98.70.Sa

1 Introduction

Cyclotron and synchrotron radiation by circularly orbiting sources is a promising radiation mechanism to scrutinize in the search for superluminal quanta, from atomic orbits via storage rings and planetary magnetospheres, to supernova remnants and pulsars [1]. The same formalism applies on vastly differing scales, set by the gyroradius, the magnetic field strength and the orbital energy of the subluminal source particles, usually electrons, muons, protons and heavier nuclei. Here, we study tachyonic line spectra of hydrogen-like ions and muonic atoms, as well as continuous X- and γ-ray spectra from electrons and protons in pulsar magnetospheres. Tachyonic γ-rays do not interact with microwave background photons, there is no absorption by electron–positron creation, in stark contrast to photonic γ-rays. This aside, the observed GeV-cutoff in the spectra of γ-ray pulsars provides evidence for gyration energies in the surface fields way beyond the 10^{19} eV mark in the cosmic ray spectrum [3].

There are substantial differences between tachyonic cyclotron/synchrotron radiation and its electromagnetic counterpart. Tachyonic quanta can be longitudinally polarized due to their negative mass square; there is a longitudinal counterpart to the transversal spectral densities. As for atomic line spectra, we will determine the power transversally and longitudinally radiated by the tachyonic cyclotron mechanism, for which there is no electromagnetic analogue at all. In the ultra-relativistic synchrotron limit, the transversal tachyonic spectral density is peaked close to the tachyon mass at 2 keV and has a slowly decaying tail, which extends well into the GeV region in high magnetic fields. In contrast, the electromagnetic spectral peak close to the critical photon frequency is followed by rapid exponential decay. In the non-relativistic limit of slowly orbiting sources, electromagnetic cyclotron radiation gives rise to line spectra, radiated in multiples of the fundamental frequency. The tachyonic counterpart admits an additional asymptotic spectral parameter, the ratio of tachyon mass and gyrofrequency, that determines whether the spectrum is discrete or continuous. The most far-reaching difference is perhaps the absence of radiation damping outside the lightcone. The Green function of the superluminal radiation field is time symmetric; there is no retarded propagator for superluminal wave propagation. The advanced component of the time symmetric radiation field is turned into the missing half of the retarded field by virtue of a non-local interaction with a cosmic absorber field, that supplies the energy of the tachyonic quanta [4, 5]. There is no slowing-down of the radiating source by radiation loss, and there is even residual radiation in the limit of infinite gyroradius, from particles in straight uniform motion. The cosmic absorber provides a distinguished frame of reference, a frame of absolute rest, indispensable to render superluminal signal transfer causal. The conceptual consequences of the cosmic absorber are summarized in the conclusions in Sect. 6.

In Sect. 2, we outline tachyonic cyclotron/synchrotron radiation theory, and state the multipole expansion of the

[a] e-mail: roman@geminga.org

transversal and longitudinal flux vectors and power components. In Sect. 3, we study tachyonic cyclotron radiation from hydrogen-like systems. We consider semiclassical circular orbits, identify the Bohr radius with the gyroradius, and infer the gyrofrequency from the orbital speed. Line spectra arise if the tachyon mass is much smaller than the gyration frequency. We calculate the power radiated from hydrogenic ions and muonic atoms, covering a wide Z-range.

In Sect. 4, we study tachyonic continuum emission, extending the ultra-relativistic synchrotron densities [1] into the mildly relativistic regime, and derive the condition for a continuous tachyonic cyclotron spectrum at non-relativistic orbital speed. We introduce the energy scales, the break and critical frequencies defining the global features of the broadband spectrum, such as spectral peaks, oscillations and decay properties. In Sect. 5, we investigate tachyonic synchrotron and cyclotron radiation from charges cycling in the surface and light cylinder fields of γ-ray pulsars. We calculate the break and critical frequencies in the tachyonic wideband spectrum, and explain how the maximal gyration energy sustainable by the pulsars can be inferred from the cutoff in the γ-ray spectrum. In Sect. 6, we present our conclusions.

2 Tachyonic cyclotron radiation: multipoles, power and polarization

We consider a constant magnetic field $\mathbf{B} = (0, 0, B)$, $B > 0$, and an electron or muon with constant speed v, electric charge e, and tachyonic charge q on a circular orbit [1]. The equations of motion read $\mathrm{d}(\gamma m_{e,\mu}\mathbf{v})/\mathrm{d}t = (-e/c)\mathbf{v}\times\mathbf{B}$, where $\gamma = (1 - v^2/c^2)^{-1/2}$ and $e > 0$. We thus find the orbit $\mathbf{x}(t) = (v/\omega_B)(\cos(\omega_B t), \sin(\omega_B t), 0)$, with gyrofrequency $\omega_B := eB/(m_{e,\mu}c\gamma)$. Gyroradius and gyrofrequency are related by $r = v/\omega_B$. Taking into account that $1\ \mathrm{kG}\cdot e \approx 0.29979\ \mathrm{MeV/cm}$, we find

$$B\,[\mathrm{G}] \approx 1.6904\times 10^{14} E\,[\mathrm{MeV}]\hbar\omega_B\,[\mathrm{MeV}],$$
$$r[\text{Å}] \approx \frac{1.9733}{\hbar\omega_B\,[\mathrm{keV}]}\frac{v}{c}, \tag{2.1}$$

where $E = m_{e,\mu}c^2\gamma$ is the energy of the orbiting electron, muon, etc. Clearly, $eB = (v/c)E/r$. We use the Heaviside–Lorentz system, in particular, $e^2/(4\pi\hbar c) =: \alpha_e \approx 1/137$ and $q^2/(4\pi\hbar c) =: \alpha_q \approx 1.0\times 10^{-13}$ are the electric and tachyonic fine structure constants. The tachyon mass, $m_t \approx 2.15\,\mathrm{keV}/c^2$, gives a Compton wavelength of $\lambda_t^{\mathrm{C}} = 2\pi\hbar/(m_t c) \approx 5.767\,\text{Å}$, and the quotient of tachyonic and electric fine structure constant reads $\alpha_q/\alpha_e \approx 1.4\times 10^{-11}$, all inferred from Lamb shifts in hydrogenic systems [6]. Tachyonic energy $\hbar\omega$ and wavelength are related by

$$\lambda_t = \frac{2\pi\hbar c}{\sqrt{m_t^2c^4 + \hbar^2\omega^2}},\quad \lambda_t\,[\text{Å}] = \frac{0.012398}{\sigma\hbar\omega\,[\mathrm{MeV}]},$$
$$\sigma := \sqrt{1 + \frac{m_t^2c^4}{\hbar^2\omega^2}}. \tag{2.2}$$

λ_t^{C} is apparently the largest possible wavelength a tachyon can attain. σ is the speed v_t/c of the tachyonic quanta, according to $\hbar\omega = m_t c^2(v_t^2/c^2 - 1)^{-1/2}$. The critical field for quantum effects to emerge is [7–11],

$$B_{\mathrm{c},e} = \frac{m_e^2c^3}{e\hbar} \approx 4.414\times 10^{13}\,\mathrm{G},$$
$$B_{\mathrm{c},\mu} = \frac{m_\mu^2}{m_e^2}B_{\mathrm{c,e}} \approx 1.887\times 10^{18}\,\mathrm{G}, \tag{2.3}$$

for orbiting electrons and muons, respectively.

We put $\hbar = c = 1$, denote the tachyonic wave vector by $\mathbf{k} = k(\omega)\mathbf{k}_0$, with $k(\omega) = \sqrt{\omega^2 + m_t^2}$, and define two further polarization unit vectors,

$$\boldsymbol{\varepsilon}_\parallel := \frac{\mathbf{B} - \mathbf{k}_0(\mathbf{k}_0\cdot\mathbf{B})}{|\mathbf{B} - \mathbf{k}_0(\mathbf{k}_0\cdot\mathbf{B})|},\quad \boldsymbol{\varepsilon}_\perp := \boldsymbol{\varepsilon}_\parallel\times\mathbf{k}_0, \tag{2.4}$$

so that $\mathbf{k}_0$, $\boldsymbol{\varepsilon}_\parallel$ and $\boldsymbol{\varepsilon}_\perp$ constitute an orthonormal triad, and $\boldsymbol{\varepsilon}_\parallel = -\boldsymbol{\varepsilon}_\perp\times\mathbf{k}_0$. Tachyonic synchrotron radiation from helically moving sources has been studied in [1]; the general setting [5] is sketched in Sect. 6. Here, we just state the flux vectors, specialized to circular motion. The frequencies radiated are $\omega_n := n\omega_B$, with positive integer n. The Poynting vectors defining the transversal and longitudinal flux through a sphere of radius r are

$$\left\langle \mathbf{S}^{\mathrm{T}}_{\parallel,\perp}\right\rangle \sim \frac{q^2\mathbf{n}}{8\pi^2r^2}\sum_{n=1}^{\infty}\left\langle s^{\mathrm{T}}_{\parallel,\perp}\right\rangle_n,$$
$$\left\langle \mathbf{S}^{\mathrm{L}}\right\rangle \sim \frac{q^2\mathbf{n}}{8\pi^2r^2}\sum_{n=1}^{\infty}\left\langle s^{\mathrm{L}}\right\rangle_n. \tag{2.5}$$

The total transversal flux, $\langle\mathbf{S}^{\mathrm{T}}\rangle = \langle\mathbf{S}^{\mathrm{T}}_\parallel\rangle + \langle\mathbf{S}^{\mathrm{T}}_\perp\rangle$, is generated by the linearly polarized components of the tachyonic radiation field defined by $\boldsymbol{\varepsilon}_{\parallel,\perp}$ in (2.4) ($\mathbf{n}$ is the coordinate unit vector). The flux components radiated at ω_n in the (rearranged) multipole expansions (2.5) read

$$\left\langle s^{\mathrm{T}}_\parallel\right\rangle_n = \cot^2\theta\frac{\omega_B^3n^3}{k(\omega_n)}J_n^2(z_n),$$
$$\left\langle s^{\mathrm{T}}_\perp\right\rangle_n = v^2\omega_B n k(\omega_n)J'^2_n(z_n),$$
$$\left\langle s^{\mathrm{L}}\right\rangle_n = m_t^2\frac{\omega_B n}{k(\omega_n)}J_n^2(z_n),$$
$$z_n := \frac{v}{\omega_B}k(\omega_n)\sin\theta, \tag{2.6}$$

where $k(\omega_n) = \sqrt{n^2\omega_B^2 + m_t^2}$ is the tachyonic wave number and θ the polar angle (polar axis $\mathbf{B}$). The power transversally and longitudinally radiated is thus

$$P^{\mathrm{T}}_{\parallel,\perp} = 2\pi r^2\int_0^\pi\left\langle\mathbf{S}^{\mathrm{T}}_{\parallel,\perp}\cdot\mathbf{n}\right\rangle\sin\theta\mathrm{d}\theta,$$
$$P^{\mathrm{L}} = 2\pi r^2\int_0^\pi\left\langle\mathbf{S}^{\mathrm{L}}\cdot\mathbf{n}\right\rangle\sin\theta\mathrm{d}\theta. \tag{2.7}$$

The total transversal power reads $P^{\mathrm{T}} = P^{\mathrm{T}}_\parallel + P^{\mathrm{T}}_\perp$, and the total power radiated is $P = P^{\mathrm{T}} + P^{\mathrm{L}}$. Interchanging

summation and integration, we may write

$$P^{\mathrm{T}}_{\parallel,\perp} = \sum_{n=1}^{\infty} \langle p^{\mathrm{T}}_{\parallel,\perp}\rangle_n, \qquad P^{\mathrm{L}} = \sum_{n=1}^{\infty} \langle p^{\mathrm{L}}\rangle_n, \quad (2.8)$$

$$\langle p^{\mathrm{T,L}}_{\parallel,\perp}\rangle_n := \frac{q^2}{4\pi}\int_0^{\pi} \langle s^{\mathrm{T,L}}_{\parallel,\perp}\rangle_n \sin\theta \mathrm{d}\theta,$$

$$\langle p^{\mathrm{T}}\rangle_n := \langle p^{\mathrm{T}}_{\parallel}\rangle_n + \langle p^{\mathrm{T}}_{\perp}\rangle_n, \quad (2.9)$$

where the power components $\langle p^{\mathrm{T}}_{\parallel,\perp}\rangle_n$ and $\langle p^{\mathrm{L}}\rangle_n$ are radiated in the nth harmonic $n\omega_B$. The energy radiated is drained from the absorber field that breaks the time symmetry of the Green function (half-advanced, half-retarded) outside the lightcone; cf. [4, 5] and Sect. 6. The radiating particles do not slow down, and they even radiate in uniform motion ($\omega_B \to 0$). In the next section, we discuss tachyonic line spectra and derive explicit asymptotic formulas for the total power and the power radiated at the individual frequencies. In Sect. 4, we derive the spectral densities of the continuum radiation, based on the power components (2.9).

3 Tachyonic line spectra of hydrogenic ions and muonic atoms

We study tachyonic cyclotron radiation in the limit $m_t^2c^4/(\hbar\omega_B)^2 \ll 1$. The notation is explained in Sect. 2, and the opposite limit is dealt with in Sect. 4. The orbital speed υ may be relativistic as long as the Lorentz factor stays moderate (since $\omega_B \propto 1/\gamma$). This condition for line spectra is met in heavy hydrogenic ions or muonic atoms [12,13], where the orbital Lorentz factor does not exceed 2. In Sect. 3.2, we will also discuss the non-relativistic limit, where a moderate $m_t^2c^4/(\hbar\omega_B)^2$ ratio is still admissible.

The gyration radii and frequencies are obtained by Bohr–Sommerfeld quantization. To this end, we start with the relativistic Coulomb problem. Solving the Hamilton–Jacobi equation, we find the action $S = -\tilde{E}t + M\varphi + S(r)$, where

$$S(r) = \int_{r_{\min}}^{r} \left[2m_{\mathrm{r}}\left(\tilde{E}+\frac{\tilde{\alpha}}{r}\right) - \frac{M^2}{r^2} + \frac{1}{c^2}\left(\tilde{E}+\frac{\tilde{\alpha}}{r}\right)^2\right]^{1/2} \mathrm{d}r. \quad (3.1)$$

We consider an attractive Coulomb potential, assuming $m_{\mathrm{r}}c^2 > \tilde{E} > 0$, $\tilde{\alpha} > 0$; more specifically, $\tilde{\alpha} = Ze^2/(4\pi)$, where e is the electronic charge so that $\alpha = e^2/(4\pi\hbar c) \approx 1/137$. Z is the charge number of the nucleus and m_{r} the reduced mass. $r_{\max\,/\,\min}$ denotes the two positive roots of the integrand,

$$r_{\max\,/\,\min} = \frac{\tilde{\alpha}\tilde{E}(1\pm\varepsilon)}{m_{\mathrm{r}}^2c^4 - \tilde{E}^2}, \quad (3.2)$$

$$\varepsilon := \left[1 - \frac{\left(m_{\mathrm{r}}^2c^4 - \tilde{E}^2\right)}{\tilde{E}^2}\left(\frac{c^2M^2}{\tilde{\alpha}^2} - 1\right)\right]^{1/2}.$$

We consider circular orbits, $\varepsilon = 0$, and find via (3.2)

$$\tilde{E} = m_{\mathrm{r}}c^2\left(1 - \frac{\tilde{\alpha}^2}{c^2M^2}\right)^{1/2} = m_{\mathrm{r}}c^2 - \frac{1}{2}\frac{m_{\mathrm{r}}\tilde{\alpha}^2}{M^2} + \ldots \quad (3.3)$$

If we insert this in turn into $r_{\min\,/\,\max}$, we obtain the orbital radius,

$$r = \frac{M^2}{m_{\mathrm{r}}\tilde{\alpha}}\left(1 - \frac{\tilde{\alpha}^2}{c^2M^2}\right)^{1/2}. \quad (3.4)$$

Energy conservation amounts to constant $\tilde{E} = m_{\mathrm{r}}c^2\gamma - \tilde{\alpha}/r$, where $\gamma = (1-\upsilon^2/c^2)^{-1/2}$ is the electronic or muonic Lorentz factor. If we equate this with $\tilde{E}$ in (3.3) and substitute the orbital radius r in (3.4), we find the orbital velocity as $\upsilon = \tilde{\alpha}/M$.

Bohr–Sommerfeld quantization means to put $S(r_{\max}) = \pi\hbar n_r$ and $M = \hbar n_\varphi$, where n_r and n_φ are the radial and azimuthal quantum numbers, adding up to the principal quantum number $n_r + n_\varphi$. Zero eccentricity implies $n_r = 0$, so that n_φ coincides with the principal quantum number. (n_φ is not to be confused with the index n labeling multipole contributions to the tachyonic flux vectors.) The energy levels obtained from the Dirac equation in a Coulomb potential coincide with (3.3), if we identify $n_\varphi = j + 1/2 = 1, 2\ldots$ The gyrofrequency relates to the quantized velocities and orbital radii as $\omega_B = \upsilon/r$. Hence,

$$\hbar\omega_B = m_{\mathrm{r}}c^2\frac{\alpha_Z^2\gamma}{n_\varphi^3}, \quad r = \frac{\hbar}{m_{\mathrm{r}}c}\frac{n_\varphi^2}{\alpha_Z\gamma}, \quad \frac{\upsilon}{c} = \frac{\alpha_Z}{n_\varphi}, \quad (3.5)$$

where $\alpha_Z \approx Z/137$ and $\gamma = (1-\alpha_Z^2/n_\varphi^2)^{-1/2}$ is the Lorentz factor of the orbiting particle. We will focus on the ground state, $n_\varphi = 1$, so that the Bohr radius reads

$$r\,[\mathrm{fm}] \approx \frac{197.327}{m_{\mathrm{r}}c^2\,[\mathrm{MeV}]}\frac{\sqrt{1-\alpha_Z^2}}{\alpha_Z}. \quad (3.6)$$

The quantities in (3.5) and (3.6) are listed in Tables 1 and 2 for some hydrogen-like ions and muonic atoms. Heavy hydrogenic ions already give a small $m_t^2c^4/(\hbar\omega_B)^2$ ratio, but this condition is more easily satisfied, and even for light ions, if the electron is replaced by a muon. The reduced electron or muon mass, $m_{e,\mu}/(1 + m_{e,\mu}/m_A)$, is denoted by $m_{\mathrm{r},e}$ and $m_{\mathrm{r},\mu}$, respectively. Here, m_A is the nuclear mass taken as A atomic mass units, $A \cdot 931.494\,\mathrm{MeV}/c^2$, plus mass excess $M - A$ as listed in [14], minus $Z \cdot m_e$. The muon mass is $m_\mu \approx 105.66\,\mathrm{MeV}/c^2$. We note the muon/electron mass ratio, $m_\mu/m_e \approx 206.77$, the tachyon/muon ratio, $m_t/m_\mu \approx 2.035 \times 10^{-5}$, and the tachyon/electron ratio, $m_t/m_e \approx 4.207 \times 10^{-3} \approx 1/238$. In the subsequent calculations, we put $\hbar = c = 1$.

3.1 The power radiated at large gyrofrequency

We start with the m_t^2/ω_B^2-expansion of the squared Bessel functions in (2.6),

$$J_n^2(z_n) = J_n^2(n\eta)\left(1 + \frac{1}{2}\frac{m_t^2\upsilon}{n^2\omega_B^2}\frac{\partial}{\partial\upsilon}\log J_n^2(n\eta) + \ldots\right), \quad (3.7)$$

Table 1. Parameters determining tachyonic cyclotron spectra. Reduced electron/muon mass $m_{\rm r}c^2$, cf. after (3.6), ground state gyrofrequency $\hbar\omega_{\rm B}$, cf. (3.5), speed σ_n of tachyonic quanta radiated at frequency $n\omega_{\rm B}$ (a shortcut for $v_t(\omega_{\rm n})/c$ used throughout Sect. 3); cf. (2.2) and (3.19). The listed tachyon-mass over gyrofrequency ratio determines whether the radiated spectrum is discrete or continuous; cf. the beginning of Sect. 3 and the end of Sect. 4.2

	$m_{\rm r}c^2$ (MeV)	$\hbar\omega_{\rm B}$ (MeV)	$\left(\frac{m_{\rm t}c^2}{\hbar\omega_{\rm B}}\right)^2$	σ_1-1	σ_2-1
Hydrogenic ions					
H	0.51072	2.7197×10^{-5}	6249	78.06	38.54
$^4\mathrm{He}^+$	0.51093	1.0884×10^{-4}	390.2	18.78	8.927
$^{24}\mathrm{Mg}^{11+}$	0.51099	3.9335×10^{-3}	0.2988	0.1396	0.03667
$^{56}\mathrm{Fe}^{25+}$	0.51099	0.018735	0.01317	6.563×10^{-3}	1.645×10^{-3}
$^{138}\mathrm{Ba}^{55+}$	0.51100	0.093498	5.288×10^{-4}	2.644×10^{-4}	6.610×10^{-5}
$^{208}\mathrm{Pb}^{81+}$	0.51100	0.22837	8.864×10^{-5}	4.432×10^{-5}	1.108×10^{-5}
$^{238}\mathrm{U}^{91+}$	0.51100	0.31076	4.786×10^{-5}	2.393×10^{-5}	5.983×10^{-6}
Muonic atoms					
$p\mu^-$	94.966	5.0572×10^{-3}	0.1807	0.08662	0.02234
$^4\mathrm{He}^{++}\mu^-$	102.75	0.021888	9.649×10^{-3}	4.813×10^{-3}	1.205×10^{-3}
$^{24}\mathrm{Mg}^{12+}\mu^-$	105.16	0.80952	7.054×10^{-6}	3.527×10^{-6}	8.817×10^{-7}
$^{56}\mathrm{Fe}^{26+}\mu^-$	105.45	3.8660	3.093×10^{-7}	1.546×10^{-7}	3.866×10^{-8}
$^{138}\mathrm{Ba}^{56+}\mu^-$	105.57	19.317	1.239×10^{-8}	6.194×10^{-9}	1.549×10^{-9}
$^{208}\mathrm{Pb}^{82+}\mu^-$	105.60	47.194	2.075×10^{-9}	1.038×10^{-9}	2.594×10^{-10}
$^{238}\mathrm{U}^{92+}\mu^-$	105.61	64.226	1.121×10^{-9}	5.603×10^{-10}	1.401×10^{-10}

Table 2. Tachyonic cyclotron radiation, semiclassical orbits, and the magnetic field analogy. Ground state Bohr radius r, cf. (3.6), tachyonic wavelength $\lambda_t(\omega_{\rm B})$ at gyrofrequency (the first harmonic radiated), cf. (2.2), electronic/muonic orbital speed v (in ground state), cf. (3.5), and corresponding Lorentz factor γ, magnetic field B sustaining a gyrofrequency $\omega_{\rm B}$ and orbital energy $E=m_{e,\mu}c^2\gamma$ (in the absence of a Coulomb potential); cf. (2.1)

	$r(n_\varphi=1)$ (fm)	$\lambda_t(\omega_{\rm B})$ (Å)	B (G)	v/c	$\gamma-1$
Hydrogenic ions					
H	52945	5.766	2.349×10^{9}	7.2974×10^{-3}	2.663×10^{-5}
$^4\mathrm{He}^+$	26460	5.759	9.403×10^{9}	0.014595	1.065×10^{-4}
$^{24}\mathrm{Mg}^{11+}$	4393.0	2.766	3.411×10^{11}	0.087568	3.856×10^{-3}
$^{56}\mathrm{Fe}^{25+}$	1998.3	0.6575	1.648×10^{12}	0.18973	0.01850
$^{138}\mathrm{Ba}^{55+}$	862.45	0.1326	8.849×10^{12}	0.40865	0.09566
$^{208}\mathrm{Pb}^{81+}$	517.05	0.05429	2.462×10^{13}	0.59838	0.2481
$^{238}\mathrm{U}^{91+}$	426.29	0.03990	3.622×10^{13}	0.67136	0.3493
Muonic atoms					
$p\mu^-$	284.74	2.256	9.033×10^{13}	7.2974×10^{-3}	2.663×10^{-5}
$^4\mathrm{He}^{++}\mu^-$	131.58	0.5637	3.910×10^{14}	0.014595	1.065×10^{-4}
$^{24}\mathrm{Mg}^{12+}\mu^-$	21.346	0.01532	1.451×10^{16}	0.087568	3.856×10^{-3}
$^{56}\mathrm{Fe}^{26+}\mu^-$	9.6840	3.207×10^{-3}	7.033×10^{16}	0.18973	0.01850
$^{138}\mathrm{Ba}^{56+}\mu^-$	4.1745	6.418×10^{-4}	3.780×10^{17}	0.40865	0.09566
$^{208}\mathrm{Pb}^{82+}\mu^-$	2.5020	2.627×10^{-4}	1.052×10^{18}	0.59838	0.2481
$^{238}\mathrm{U}^{92+}\mu^-$	2.0627	1.930×10^{-4}	1.548×10^{18}	0.67136	0.3493

where $\eta := v\sin\theta$, and the same for ${J'}^2_n(z_n)$. In this way we can expand the transversal flux components $\langle s^{\rm T}_{\parallel,\perp}\rangle_n$ in (2.5) as

$$\begin{aligned}\big\langle s^{\rm T}_\parallel\big\rangle_n &= n^2\omega_B^2\cot^2\theta J_n^2(n\eta)\\ &\quad+\frac{1}{2}m_t^2\cot^2\theta\left(v\frac{\partial J_n^2(n\eta)}{\partial v}-J_n^2(n\eta)\right)+O(m_t^4),\\ \big\langle s^{\rm T}_\perp\big\rangle_n &= n^2\omega_B^2v^2{J'}^2_n(n\eta)\\ &\quad+\frac{1}{2}m_t^2v^2\left(v\frac{\partial {J'}^2_n(n\eta)}{\partial v}+{J'}^2_n(n\eta)\right)+O(m_t^4).\end{aligned}\tag{3.8}$$

The longitudinal flux at ω_n reads

$$\big\langle s^{\rm L}\big\rangle_n = m_t^2J_n^2(n\eta)+O(m_t^4).\tag{3.9}$$

The multipole summations in (2.5) can be reduced to Kapteyn series [15],

$$\begin{aligned}K_0&:=\sum_{n=1}^\infty J_n^2(n\eta)=\frac{1}{2}\frac{1}{\sqrt{1-\eta^2}}-\frac{1}{2},\\ K_2&:=\sum_{n=1}^\infty n^2J_n^2(n\eta)=\frac{\eta^2(\eta^2+4)}{16(1-\eta^2)^{7/2}},\\ K_{-2}&:=\sum_{n=1}^\infty n^{-2}J_n^2(n\eta)=\frac{\eta^2}{4}.\end{aligned}\tag{3.10}$$

By applying the identity

$${J'}^2_n(nz)=\left[\frac{1}{2n^2}\left(\frac{{\rm d}^2}{{\rm d}z^2}+\frac{\rm d}{z{\rm d}z}\right)+1-\frac{1}{z^2}\right]J_n^2(nz),\tag{3.11}$$

we obtain

$$\begin{aligned}K_0^{(1)}&:=\sum_{n=1}^\infty {J'}^2_n(n\eta)=\frac{1-\sqrt{1-\eta^2}}{2\eta^2},\\ K_2^{(1)}&:=\sum_{n=1}^\infty n^2{J'}^2_n(n\eta)=\frac{4+3\eta^2}{16(1-\eta^2)^{5/2}},\end{aligned}\tag{3.12}$$

and we note

$$\begin{aligned}v\frac{\partial K_0}{\partial v}&=\frac{\eta^2}{2(1-\eta^2)^{3/2}},\\ v\frac{\partial K_0^{(1)}}{\partial v}&=\left(\frac{1}{\eta^2}-\frac{1}{2}\right)\frac{1}{\sqrt{1-\eta^2}}-\frac{1}{\eta^2}.\end{aligned}\tag{3.13}$$

The transversal flux components can thus be summed to

$$\begin{aligned}\sum_{n=1}^\infty\big\langle s^{\rm T}_\parallel\big\rangle_n &= \frac{\omega_B^2}{16}\cot^2\theta\frac{\eta^2(\eta^2+4)}{(1-\eta^2)^{7/2}}\\ &\quad+\frac{m_t^2}{4}\cot^2\theta\left(\frac{\eta^2}{(1-\eta^2)^{3/2}}-\frac{1}{\sqrt{1-\eta^2}}+1\right)\\ &\quad+O\left(\frac{m_t^4}{\omega_B^2}\right),\end{aligned}$$

$$\begin{aligned}\sum_{n=1}^\infty\big\langle s^{\rm T}_\perp\big\rangle_n &= \frac{\omega_B^2v^2}{16}\frac{3\eta^2+4}{(1-\eta^2)^{5/2}}\\ &\quad+\frac{m_t^2}{4\sin^2\theta}\left(\frac{1}{\sqrt{1-\eta^2}}-1\right)+O\left(\frac{m_t^4}{\omega_B^2}\right),\end{aligned}\tag{3.14}$$

and the longitudinal summation gives

$$\sum_{n=1}^\infty\big\langle s^{\rm L}\big\rangle_n=\frac{m_t^2}{2}\left(\frac{1}{\sqrt{1-\eta^2}}-1+O\left(\frac{m_t^2}{\omega_B^2}\right)\right).\tag{3.15}$$

The integrations in (2.7) are elementary if we use (3.14) and (3.15), with $\eta=v\sin\theta$. The transversal power components in (2.7) can be assembled as

$$\begin{aligned}P^{\rm T}_\parallel&=\frac{q^2}{4\pi}\omega_B^2\bigg[\frac{v^2(2-v^2)}{12(1-v^2)^2}\\ &\quad+\frac{m_t^2}{\omega_B^2}\left(\frac{1}{2v}\log\frac{1+v}{1-v}+\frac{1}{4}\log(1-v^2)-1\right)\\ &\quad+O\left(\frac{m_t^4}{\omega_B^4}\right)\bigg],\\ P^{\rm T}_\perp&=\frac{q^2}{4\pi}\omega_B^2\bigg[\frac{v^2(6+v^2)}{12(1-v^2)^2}-\frac{1}{4}\frac{m_t^2}{\omega_B^2}\log(1-v^2)\\ &\quad+O\left(\frac{m_t^4}{\omega_B^4}\right)\bigg].\end{aligned}\tag{3.16}$$

Restoring units, we may write $P^{\rm T}=P^{\rm T}_\parallel+P^{\rm T}_\perp$ as

$$\begin{aligned}P^{\rm T}&=\alpha_q\hbar\omega_B^2\bigg[\frac{2}{3}\frac{v^2/c^2}{(1-v^2/c^2)^2}\\ &\quad+\frac{m_t^2c^4}{\hbar^2\omega_B^2}\left(\frac{c}{2v}\log\frac{1+v/c}{1-v/c}-1\right)+O\left(\frac{m_t^4}{\omega_B^4}\right)\bigg],\end{aligned}\tag{3.17}$$

where $\alpha_q=q^2/(4\pi\hbar c)$ is the tachyonic fine structure constant defined after (2.1). The longitudinally radiated power (2.7) reads

$$P^{\rm L}=\alpha_q\frac{m_t^2c^4}{\hbar}\left(\frac{1}{2}\frac{c}{v}\log\frac{1+v/c}{1-v/c}-1+O\left(\frac{m_t^2}{\omega_B^2}\right)\right).\tag{3.18}$$

These powers $P^{\rm T,L}$ are listed in Table 3 for various hydrogenic ions and muonic atoms.

3.2 The power radiated at small orbital velocity

We turn to non-relativistic orbital velocities, and calculate the power radiated in a v^2/c^2-expansion. We define, cf. (2.2),

$$k(\omega_n)=\frac{n\omega_B}{c}\sigma_n,\qquad \sigma_n:=\sqrt{1+\frac{m_t^2c^4}{\hbar^2\omega_B^2n^2}},\tag{3.19}$$

and we will occasionally write k_n for $k(\omega_n)$, $\omega_n=n\omega_B$. The expansion parameter turns out to be $\sigma_1 v/c$ squared,

Table 3. The power superluminally radiated. Transversal/longitudinal power $\langle p^{\mathrm{T,L}}\rangle_1$ radiated at the fundamental frequency ω_{B}, power $\langle p^{\mathrm{T,L}}\rangle_2$ radiated at the second harmonic $2\omega_{\mathrm{B}}$, cf. (3.24) and (3.26), total power $P^{\mathrm{T,L}}$ transversally/longitudinally radiated, calculated via (3.17) and (3.18). The extend to which $\langle p^{\mathrm{T,L}}\rangle_1$ and $\langle p^{\mathrm{T,L}}\rangle_2$ add up to $P^{\mathrm{T,L}}$ indicates the quality of the non-relativistic approximation (3.25) and (3.27), which apparently breaks down for the ^{208}Pb and ^{238}U ground states

	$\langle p^{\mathrm{T}}\rangle_1$ (MeV s^{-1})	$\langle p^{\mathrm{T}}\rangle_2$ (MeV s^{-1})	$\langle p^{\mathrm{L}}\rangle_1$ (MeV s^{-1})	$\langle p^{\mathrm{L}}\rangle_2$ (MeV s^{-1})	P^{T} (MeV s^{-1})	P^{L} (MeV s^{-1})
Hydrogenic ions						
H	2.734×10^{-4}	3.152×10^{-5}	0.9199	0.03283	–	–
^{4}He$^+$	4.887×10^{-3}	1.278×10^{-4}	0.9698	8.313×10^{-3}	–	–
^{24}Mg^{11+}	13.64	0.2464	2.042	0.01227	14.01	1.803
^{56}Fe^{25+}	1270	111.1	8.420	0.2439	1386	8.614
^{138}Ba^{55+}	1.380×10^{5}	5.927×10^{4}	37.80	5.224	2.131×10^{5}	43.55
^{208}Pb^{81+}	1.620×10^{6}	1.625×10^{6}	77.82	24.01	4.590×10^{6}	108.3
^{238}U^{91+}	3.614×10^{6}	4.769×10^{6}	96.00	38.05	1.461×10^{7}	148.4
Muonic atoms						
$p\mu^-$	0.1499	1.884×10^{-5}	0.01355	5.675×10^{-7}	0.1511	0.01317
^{4}He$^{++}\mu^-$	10.38	5.303×10^{-3}	0.05010	8.528×10^{-6}	10.39	0.04940
^{24}Mg$^{12+}\mu^-$	5.074×10^{5}	9.367×10^{3}	1.792	0.01101	5.169×10^{5}	1.803
^{56}Fe$^{26+}\mu^-$	5.371×10^{7}	4.708×10^{6}	8.366	0.2427	5.864×10^{7}	8.614
^{138}Ba$^{56+}\mu^-$	5.890×10^{9}	2.530×10^{9}	37.79	5.223	9.096×10^{9}	43.55
^{208}Pb$^{82+}\mu^-$	6.921×10^{10}	6.941×10^{10}	77.82	24.01	1.960×10^{11}	108.3
^{238}U$^{92+}\mu^-$	1.544×10^{11}	2.037×10^{11}	96.00	38.04	6.241×10^{11}	148.4

cf. (3.23), (3.25) and (3.27), which imposes a restriction on the size of the ratio $m_tc^2/(\hbar\omega_B)$.

We start with the v/c-expansion of the flux components (2.6). In this limit, we can use the ascending series of the squared Bessel functions,

$$\begin{aligned}
J_1^2(z) &= (z^2/4)(1-z^2/4+\ldots),\\
J_2^2(z) &= (z^4/64)+\ldots,\\
J_n^2(z) &= O(z^{2n}),\\
J'^2_1(z) &= 1/4(1-3z^2/4+\ldots),\\
J'^2_2(z) &= z^2/16+\ldots,\\
J'^2_n(z) &= O(z^{2n-2}),
\end{aligned}\tag{3.20}$$

so that the first two flux components (radiated at ω_B and $2\omega_B$) give

$$\begin{aligned}
\langle s^{\mathrm{T}}_{\parallel}\rangle_{1+2} &= \frac{1}{4}\omega_B v^2 k_1\cos^2\theta\\
&\quad\times\left[1+\left(\frac{1}{2}\frac{k_2^3}{k_1}-\frac{1}{4}k_1^2\right)\frac{v^2}{\omega_B^2}\sin^2\theta+O(v^4)\right],\\
\langle s^{\mathrm{T}}_{\perp}\rangle_{1+2} &= \frac{1}{4}\omega_B v^2 k_1\\
&\quad\times\left[1+\left(\frac{1}{2}\frac{k_2^3}{k_1}-\frac{3}{4}k_1^2\right)\frac{v^2}{\omega_B^2}\sin^2\theta+O(v^4)\right],
\end{aligned}\tag{3.21}$$

where $k_n=k(n\omega_B)$ and $\hbar=c=1$. Only the k_2^3-terms stem from $\langle s^{\mathrm{T}}_{\parallel,\perp}\rangle_2$, and the components $\langle s^{\mathrm{T}}_{\parallel,\perp}\rangle_n$, $n>2$, radiated at higher frequencies $n\omega_B$, do not contribute to the Poynting vectors (2.5) in the indicated order in v. As for the longitudinal power radiated, cf. (2.6),

$$\begin{aligned}
\langle s^{\mathrm{L}}\rangle_{1+2} &= \frac{m_t^2v^2k_1}{4\omega_B}\sin^2\theta\\
&\quad\times\left[1+\left(\frac{1}{8}\frac{k_2^3}{k_1}-\frac{1}{4}k_1^2\right)\frac{v^2}{\omega_B^2}\sin^2\theta+O(v^4)\right].
\end{aligned}\tag{3.22}$$

Restoring the units, we find the transversal power, cf. (2.8) and (2.9),

$$\begin{aligned}
P^{\mathrm{T}}_{\parallel}\sim\langle p^{\mathrm{T}}_{\parallel}\rangle_{1+2} &= \frac{1}{6}\alpha_q\hbar\omega_B^2\sigma_1\frac{v^2}{c^2}\\
&\quad\times\left[1+\left(\frac{8}{5}\frac{\sigma_2^3}{\sigma_1^3}-\frac{1}{10}\right)\sigma_1^2\frac{v^2}{c^2}+O(v^4)\right],\\
P^{\mathrm{T}}_{\perp}\sim\langle p^{\mathrm{T}}_{\perp}\rangle_{1+2} &= \frac{1}{2}\alpha_q\hbar\omega_B^2\sigma_1\frac{v^2}{c^2}\\
&\quad\times\left[1+\left(\frac{8}{3}\frac{\sigma_2^3}{\sigma_1^3}-\frac{1}{2}\right)\sigma_1^2\frac{v^2}{c^2}+O(v^4)\right].
\end{aligned}\tag{3.23}$$

Only the $(\sigma_2/\sigma_1)^3$-term stems from the second harmonic, and higher frequencies do not affect the indicated order; cf. (3.20). The transversal (unpolarized) power components $\langle p^{\mathrm{T}}\rangle_n=\langle p^{\mathrm{T}}_{\parallel}\rangle_n+\langle p^{\mathrm{T}}_{\perp}\rangle_n$, radiated in the first and second harmonic,

$$\langle p^{\mathrm{T}}\rangle_1=\frac{2}{3}\alpha_q\hbar\omega_B^2\sigma_1\frac{v^2}{c^2}\left(1-\frac{2}{5}\sigma_1^2\frac{v^2}{c^2}+O(v^4)\right),$$

Table 4. Tachyonic number counts. The counts at frequency $n\omega_{\rm B}$ are calculated as $\langle n^{\rm T,L}\rangle_n = \langle p^{\rm T,L}\rangle_n/(\hbar\omega_{\rm B}n)$, cf. Sect. 3.2, with power components in the non-relativistic approximation (3.24) and (3.26); cf. Table 3. $\langle n^{\rm T,L}\rangle_1$ is the number of superluminal quanta radiated per second at gyrofrequency, likewise $\langle n^{\rm T,L}\rangle_2$, transversally/longitudinally radiated at the second harmonic. The estimates given for ^{208}Pb and ^{238}U are merely illustrative, as the charge numbers are already too high for the non-relativistic limit to apply; cf. (3.5)

	$\langle n^{\rm T}\rangle_1$ ($\rm s^{-1}$)	$\langle n^{\rm T}\rangle_2$ ($\rm s^{-1}$)	$\langle n^{\rm L}\rangle_1$ ($\rm s^{-1}$)	$\langle n^{\rm L}\rangle_2$ ($\rm s^{-1}$)
Hydrogenic ions				
H	10.05	1.159	3.382×10^4	1207
$^4He^+$	44.90	1.174	8910	76.37
$^{24}Mg^{11+}$	3468	62.64	519.0	3.119
$^{56}Fe^{25+}$	6.775×10^4	5931	449.4	13.02
$^{138}Ba^{55+}$	1.476×10^6	6.340×10^5	404.2	55.87
$^{208}Pb^{81+}$	7.096×10^6	7.117×10^6	340.8	105.1
$^{238}U^{91+}$	1.163×10^7	1.535×10^7	308.9	122.4
Muonic atoms				
$p\mu^-$	29.64	3.725×10^{-3}	2.678	1.122×10^{-4}
$^4He^{++}\mu^-$	474.4	0.2423	2.289	3.896×10^{-4}
$^{24}Mg^{12+}\mu^-$	6.268×10^5	1.157×10^4	2.214	0.01360
$^{56}Fe^{26+}\mu^-$	1.389×10^7	1.218×10^6	2.164	0.06277
$^{138}Ba^{56+}\mu^-$	3.049×10^8	1.309×10^8	1.956	0.2704
$^{208}Pb^{82+}\mu^-$	1.466×10^9	1.471×10^9	1.649	0.5088
$^{238}U^{92+}\mu^-$	2.403×10^9	3.172×10^9	1.495	0.5924

$$\langle p^{\rm T}\rangle_2 = \frac{8}{5}\alpha_q\hbar\omega_B^2\sigma_2^3\frac{\upsilon^4}{c^4}(1+O(\upsilon^2)), \tag{3.24}$$

add up to the total transversal power $P^{\rm T} = P^{\rm T}_{\parallel} + P^{\rm T}_{\perp}$,

$$P^{\rm T} = \frac{2}{3}\alpha_q\hbar\omega_B^2\sigma_1\frac{\upsilon^2}{c^2}\left[1+\left(\frac{12}{5}\frac{\sigma_2^3}{\sigma_1^3}-\frac{2}{5}\right)\sigma_1^2\frac{\upsilon^2}{c^2}+O(\upsilon^4)\right]. \tag{3.25}$$

The power components longitudinally radiated at ω_B and $2\omega_B$,

$$\langle p^{\rm L}\rangle_1 = \frac{1}{3}\frac{\alpha_q m_t^2c^4}{\hbar}\sigma_1\frac{\upsilon^2}{c^2}\left(1-\frac{1}{5}\sigma_1^2\frac{\upsilon^2}{c^2}+O(\upsilon^4)\right),$$
$$\langle p^{\rm L}\rangle_2 = \frac{4}{15}\frac{\alpha_q m_t^2c^4}{\hbar}\sigma_2^3\frac{\upsilon^4}{c^4}(1+O(\upsilon^2)), \tag{3.26}$$

result in the longitudinal power,

$$P^{\rm L} = \frac{1}{3}\frac{\alpha_q m_t^2c^4}{\hbar}\sigma_1\frac{\upsilon^2}{c^2}\left[1+\left(\frac{4}{5}\frac{\sigma_2^3}{\sigma_1^3}-\frac{1}{5}\right)\sigma_1^2\frac{\upsilon^2}{c^2}+O(\upsilon^4)\right]. \tag{3.27}$$

The longitudinal/transversal power ratio reads $P^{\rm L}/P^{\rm T}\sim m_t^2c^4/(2\hbar^2\omega_B^2)$, in leading order. As a consistency check, we note that the m_t^2/ω_B^2-expansion of the powers (3.23), (3.25) and (3.27) coincides with the υ^2-expansion of those in (3.16)–(3.18). The power components $\langle p^{\rm T,L}\rangle_{n=1,2}$ radiated in the first and second harmonic, cf. (3.24) and (3.26), are listed in Table 3. The tachyonic number count, $\langle n^{\rm T,L}\rangle_n := \langle p^{\rm T,L}\rangle_n/(\hbar\omega_B n)$ (tachyons emitted per unit time at frequency ω_n), is listed in Table 4 for the first two harmonics. The intensity of the tachyonic cyclotron lines is roughly by a factor of α_q/α_e weaker than the spontaneous electromagnetic emission intensity. Nevertheless, the longitudinal polarization and the predicted precise location of these lines can be helpful in sifting out superluminal quanta.

In the tables, we focus exclusively on ground states. Moderately excited states can be dealt with analogously, cf. (3.5), but Rydberg states result in continuous spectral densities. The quantities in Tables 1 and 2 scale as $\hbar\omega_B\propto n_\varphi^{-3}$, $\sigma_{1,2}\propto n_\varphi^3$, $r\propto n_\varphi^2$, $\lambda_t\propto 1$, $B\propto n_\varphi^{-3}$, $\upsilon/c\propto n_\varphi^{-1}$, and $\gamma-1\propto n_\varphi^{-2}$. Therefore, neither the condition $m_tc^2/(\hbar\omega_B)\ll 1$, cf. (3.17) and (3.18), nor $\sigma_1\upsilon/c\ll 1$, cf. after (3.19), can be met in highly excited states. In the next section, we consider the continuous spectrum, the classical version of tachyonic synchrotron and cyclotron radiation, which applies to orbital speeds $\upsilon/c > m_t/(2m_{{\rm e},\mu})$; otherwise quantum effects will emerge [16]. As the orbital velocities $\upsilon/c=\alpha_Z/n_\varphi$ are very low, we will not consider Rydberg atoms here.

4 Tachyonic cyclotron densities

We investigate the cross-over from the non-relativistic cyclotron to the ultra-relativistic synchrotron regime [17]. The key to the transversal and longitudinal spectral densities is the power $\langle p^{\mathrm{T,L}}_{\parallel,\perp}\rangle_n$ radiated through the individual flux components $\langle s^{\mathrm{T,L}}_{\parallel,\perp}\rangle_n$ at high n; cf. (2.9). We start with the Schott identities [18] for transversal radiation,

$$\begin{aligned} t^{\parallel}_n(x) &:= \int_0^{\pi} J_n^2(x\sin\theta)\cot^2\theta\sin\theta\mathrm{d}\theta \\ &= 2\int_0^{2x} z^{-1}J_{2n}(z)\mathrm{d}z - \frac{1}{x}\int_0^{2x} J_{2n}(z)\mathrm{d}z, \\ t^{\perp}_n(x) &:= \int_0^{\pi} {J'}_n^2(x\sin\theta)\sin\theta\mathrm{d}\theta \\ &= \frac{2}{x}{J'}_{2n}(2x) + \frac{1}{x}\int_0^{2x} J_{2n}(z)\mathrm{d}z \\ &- 2\frac{n^2}{x^2}\int_0^{2x} z^{-1}J_{2n}(z)\mathrm{d}z, \end{aligned} \tag{4.1}$$

and the longitudinal power components can be dealt with analogously,

$$l_n(x) := \int_0^{\pi} J_n^2(x\sin\theta)\sin\theta\mathrm{d}\theta = \frac{1}{x}\int_0^{2x} J_{2n}(z)\mathrm{d}z. \tag{4.2}$$

The asymptotic evaluation of these integrals depends on whether the ratio x/n is smaller or larger than 1. This separates the spectrum into a high- and low-frequency band.

4.1 High-frequency radiation

We consider the tangent (Debye) approximation of the Bessel functions in (4.1) and (4.2), assuming at first $x/n<1$, which defines the high-frequency regime. In this approximation [17,19],

$$\begin{aligned} J_{n+k}(x) \sim{}& \frac{(1-x^2/n^2)^{-1/4}}{\sqrt{2\pi n}}\left(\frac{x/n}{1+\sqrt{1-x^2/n^2}}\right)^{n+k} \\ &\times\exp\left(n\sqrt{1-x^2/n^2}\right)\left(1+O\left(\frac{1}{\tilde n}\right)\right), \end{aligned} \tag{4.3}$$

valid for $\tilde n := n(1-x^2/n^2)^{3/2}\gg 1$. Here, k is a small integer, $|k|\ll n$, and apparently $x/n<1$ is required. We note

$$\begin{aligned} {J'}_{n+k}(x) &\sim \frac{n}{x}\sqrt{1-x^2/n^2}J_{n+k}(x), \\ \int_0^x J_{n+k}(x)\mathrm{d}x &\sim \frac{x}{n}\frac{J_{n+k}(x)}{\sqrt{1-x^2/n^2}}, \\ \int_0^x \frac{J_{n+k}(x)}{x}\mathrm{d}x &\sim \frac{1}{n}\frac{J_{n+k}(x)}{\sqrt{1-x^2/n^2}}, \end{aligned} \tag{4.4}$$

where $J_n(x)$ on the right-hand side is meant in the approximation (4.3). This can easily be checked by differentiation, using the exact identities $2{J'}_n = J_{n-1}-J_{n+1}$ and $(2n/x)J_n = J_{n-1}+J_{n+1}$. We thus find, cf. (4.1),

$$\begin{aligned} t^{\parallel}_n(x) &\sim \frac{J_{2n}(2x)}{n}\cdot O\left(\frac{1}{\tilde n}\right), \\ t^{\perp}_n(x) &\sim \frac{J_{2n}(2x)}{n}\frac{n^2}{x^2}\sqrt{1-x^2/n^2}, \\ l_n(x) &\sim \frac{J_{2n}(2x)}{n\sqrt{1-x^2/n^2}}, \end{aligned} \tag{4.5}$$

with $J_{2n}(2x)$ as in (4.3). By virtue of (2.6) and (2.9),

$$\left\langle p^{\mathrm{T}}\right\rangle_n = \frac{q^2}{4\pi}\left(\frac{\omega_B^3 n^3}{c^2k(\omega_n)}t^{\parallel}_n(x) + \frac{\upsilon^2}{c^2}\omega_B n k(\omega_n)t^{\perp}_n(x)\right), \tag{4.6}$$

$$\left\langle p^{\mathrm{L}}\right\rangle_n = \frac{q^2}{4\pi}\frac{m_t^2c^2\omega_B n}{\hbar^2k(\omega_n)}l_n(x), \qquad x := \frac{\upsilon k(\omega_n)}{\omega_B}, \tag{4.7}$$

so that the above x/n ratio reads

$$\frac{x}{n} = \sigma(\omega_n)\frac{\upsilon}{c}, \qquad \sigma(\omega) := \sqrt{1+\frac{m_t^2c^4}{\hbar^2\omega^2}}. \tag{4.8}$$

σ is the speed υ_t/c of the tachyonic quanta at frequency $\omega_n := \omega_B n$, and $k(\omega) = (\omega/c)\sigma(\omega)$; cf. (3.19). The tachyonic wavelength λ_t is obtained via (2.2), by identifying $\omega=\omega_n$. This identification, the continuum limit, will be carried out whenever convenient. The condition $x/n<1$ covers the high-frequency regime, $\omega>\omega_{\mathrm{b}}$, where

$$\hbar\omega_{\mathrm{b}} := m_tc^2\sqrt{\gamma^2-1} \tag{4.9}$$

is the break energy. The low-frequency band, $\omega<\omega_{\mathrm{b}}$, is dealt with in Sect. 4.2. γ is the Lorentz factor of the orbiting source, so that $\upsilon/c = \sqrt{\gamma^2-1}/\gamma$ and $\sigma(\omega_{\mathrm{b}}) = c/\upsilon$.

We use a hyperbolic parametrization [19] of the tangent approximation (4.3), defining $\cosh\alpha_n := n/x$, $\alpha_n>0$. Hence,

$$\begin{aligned} \tanh\alpha_n &= \sqrt{1-\sigma^2(\omega_n)\frac{\upsilon^2}{c^2}}, \\ \alpha_n &= \log\frac{1+\sqrt{1-\sigma^2(\omega_n)\upsilon^2/c^2}}{\sigma(\omega_n)\upsilon/c}, \\ J_{2n}(2x) &\sim \frac{\exp(-2n(\alpha_n-\tanh\alpha_n))}{\sqrt{4\pi n\tanh\alpha_n}}. \end{aligned} \tag{4.10}$$

The criterion for the applicability of the tangent approximation stated after (4.3) reads $\omega/\omega_B\gg\gamma^3_\infty(\omega)$, where

$$\gamma_\infty(\omega) := \frac{1}{\sqrt{1-\sigma^2(\omega)\upsilon^2/c^2}} \equiv \frac{\gamma}{\sqrt{1-\omega_{\mathrm{b}}^2/\omega^2}}. \tag{4.11}$$

ω_{b} is the break frequency (4.9), and the subscript ∞ indicates the high-frequency regime $\omega>\omega_{\mathrm{b}}$.

We may thus write the densities (4.6) and (4.7) as

$$\langle p^{\mathrm{T}}\rangle_n \sim \frac{\alpha_q\hbar\omega_B^2}{2\sqrt{\pi}}\frac{\sqrt{n}}{\sigma}\frac{1}{\sqrt{\gamma_\infty}} \times \exp\left[-2n\left(\frac{1}{2}\log\frac{\gamma_\infty+1}{\gamma_\infty-1}-\frac{1}{\gamma_\infty}\right)\right], \tag{4.12}$$

$$\langle p^{\mathrm{L}}\rangle_n \sim \frac{m_t^2c^4\gamma_\infty^2}{\hbar^2\omega_B^2n^2}\langle p^{\mathrm{T}}\rangle_n, \tag{4.13}$$

where we used (4.5), (4.10) and (4.11). σ and γ_∞ are taken at ω_n, and $\alpha_q = q^2/(4\pi\hbar c)$ is the tachyonic fine structure constant as defined after (2.1). The $t_n^{\parallel}(x)$ polarization component in (4.6) does not contribute in leading order. We use a continuum approximation for the frequency, writing $\omega = \omega_n = \omega_B n$, and $\langle p^{\mathrm{T,L}}\rangle_n \mathrm{d}n \approx p_\infty^{\mathrm{T,L}}(\omega)\mathrm{d}\omega$, with the continuous spectral densities $p_\infty^{\mathrm{T,L}}(\omega) := \omega_B^{-1}\langle p^{\mathrm{T,L}}\rangle_{n=\omega/\omega_B}$. In (4.12) and (4.13), we thus put $n = \omega/\omega_B$. The tachyonic number count (tachyons emitted per unit time) is $n_\infty^{\mathrm{T,L}}(\omega) := p_\infty^{\mathrm{T,L}}(\omega)/(\hbar\omega)$.

We define, cf. (4.12),

$$\delta_\infty := 3\gamma_\infty^3\left(\frac{1}{2}\log\frac{\gamma_\infty+1}{\gamma_\infty-1}-\frac{1}{\gamma_\infty}\right),$$
$$\xi_\infty := \frac{2}{3\gamma_\infty^3}\frac{\omega}{\omega_B}\delta_\infty, \tag{4.14}$$

and keep γ fixed. If $\omega\to\omega_{\mathrm{b}}$, then $\gamma_\infty\to\infty$, cf. (4.11), and $\delta_\infty = 1+(3/5)\gamma_\infty^{-2}+\ldots$, so that $\xi_\infty\to 0$. If $\omega\to\infty$, then $\gamma_\infty\to\gamma$ and $\xi_\infty\to\infty$. To connect with the synchrotron regime, we note the ultra-relativistic spectral functions [1],

$$L_\infty(\xi) := \frac{1}{\sqrt{3}\pi}\int_\xi^\infty K_{1/3}(x)\mathrm{d}x,$$
$$F_\infty(\xi) := \frac{1}{\sqrt{3}\pi}\int_\xi^\infty K_{5/3}(x)\mathrm{d}x = \frac{2}{\sqrt{3}\pi}K_{2/3}(\xi) - L_\infty(\xi), \tag{4.15}$$

which admit the $\xi\to\infty$ limit $(F_\infty, L_\infty)(\xi)\sim(6\pi\xi)^{-1/2}\mathrm{e}^{-\xi}$. In this limit, we can identify

$$p_\infty^{\mathrm{T}}(\omega) \sim \alpha_q\hbar\omega\frac{\sqrt{\delta_\infty}}{\sigma\gamma_\infty^2}F_\infty(\xi_\infty),$$
$$p_\infty^{\mathrm{L}}(\omega) \sim \alpha_q\frac{m_t^2c^4}{\hbar\omega}\frac{\sqrt{\delta_\infty}}{\sigma}L_\infty(\xi_\infty), \tag{4.16}$$

where $\sigma(\omega)$ and $\gamma_\infty(\omega)$ are defined in (4.8) and (4.11), and δ_∞ and ξ_∞ in (4.14). These densities extend into the ultra-relativistic synchrotron regime via the exact spectral functions (4.15); cf. Sect. 4.3.

4.2 Low-frequency radiation

To obtain the spectral densities in the low-frequency band, $\omega<\omega_{\mathrm{b}}$, below the break frequency (4.9), we use the Debye approximation of the Bessel functions in (4.1) and (4.2) for $x/n>1$ [19],

$$J_{n+k}(x) \sim A_n(x)\cos B_{n,k}(x)(1+O(1/\tilde{n})),$$
$$A_n(x) := \sqrt{2/(\pi n)}(x^2/n^2-1)^{-1/4},$$
$$B_{n,k}(x) := n\left(\sqrt{x^2/n^2-1}-\arccos(n/x)\right) - \pi/4 - k\arccos(n/x). \tag{4.17}$$

This is valid for $\tilde{n} := n(x^2/n^2-1)^{3/2}\gg 1$, and $0<\arccos<\pi/2$. Analogously to (4.4),

$$J'_{n+k}(x) \sim -\frac{n}{x}\sqrt{x^2/n^2-1}A_n(x)\sin B_{n,k}(x),$$
$$\int_x^\infty J_{n+k}(z)\mathrm{d}z \sim -\frac{x}{n}\frac{A_n(x)\sin B_{n,k}(x)}{\sqrt{x^2/n^2-1}},$$
$$\int_x^\infty \frac{J_{n+k}(z)}{z}\mathrm{d}z \sim -\frac{1}{n}\frac{A_n(x)\sin B_{n,k}(x)}{\sqrt{x^2/n^2-1}}. \tag{4.18}$$

We will need these formulas only for $k=0$, but $k=\pm1$ is useful to check for consistency, if we employ the (integrated) identities for Bessel functions mentioned after (4.4). We also note $\int_0^\infty J_n(x)\mathrm{d}x = 1$ and $\int_0^\infty J_n(x)x^{-1}\mathrm{d}x = 1/n$, which allows one to rewrite the Schott identities (4.1) and (4.2) in a way that the integrals in (4.16) can be substituted. We find

$$t_n^{\parallel}(x) \sim \frac{1}{n}\left(1-\frac{n}{x}\right),$$
$$t_n^{\perp}(x) \sim \frac{1}{x}\left(1-\frac{n}{x}\right) - \frac{1}{n}\frac{n^2}{x^2}\sqrt{x^2/n^2-1}A_{2n}(2x)\sin B_{2n,0}(2x),$$
$$l_n(x) \sim \frac{1}{x}\left(1+\frac{x}{n}\frac{A_{2n}(2x)\sin B_{2n,0}(2x)}{\sqrt{x^2/n^2-1}}\right), \tag{4.19}$$

where we use $x/n = \sigma(\omega_n)v/c$, with

$$\sigma(\omega) = \sqrt{1+m_t^2c^4/(\hbar^2\omega^2)}$$

as in (4.8). The counterpart to (4.11) is the shortcut

$$\gamma_0(\omega) := \frac{1}{\sqrt{\sigma^2(\omega)v^2/c^2-1}} \equiv \frac{\gamma}{\sqrt{\omega_{\mathrm{b}}^2/\omega^2-1}}, \tag{4.20}$$

where the subscript zero indicates the low-frequency regime $x/n>1$ or $\omega<\omega_{\mathrm{b}}$, with $\omega_{\mathrm{b}} = (m_tc^2/\hbar)\sqrt{\gamma^2-1}$. The condition $\tilde{n}\gg1$ for the applicability of the tangent approximation, cf. after (4.17), reads $\omega/\omega_B\gg\gamma_0^3(\omega)$.

In (4.19), we may thus substitute,

$$A_{2n}(2x) = \sqrt{\frac{\gamma_0}{\pi n}},$$
$$B_{2n,0}(2x) = 2n\left(\frac{1}{\gamma_0}-\arctan\frac{1}{\gamma_0}\right)-\frac{\pi}{4}. \tag{4.21}$$

γ_0 is taken at ω_n, $0<\arctan<\pi/2$, and $\arccos(c/(\sigma v)) = \arctan(1/\gamma_0)$. Hence, below the break frequency ω_{b}, the spectral densities (4.6) and (4.7) can be assembled as

$$\langle p^{\mathrm{T}}\rangle_n \sim \frac{\alpha_q\hbar\omega_B^2n}{\sigma^2\gamma_0^2}\frac{c}{v}\left(1-\frac{v}{c}\frac{\sigma\gamma_0^{3/2}}{\sqrt{\pi n}}\sin B_{2n,0}\right), \tag{4.22}$$

$$\left\langle p^{\mathrm{L}}\right\rangle_n \sim \frac{\alpha_q m_t^2 c^4}{\hbar n \sigma^2}\frac{c}{\upsilon}\left(1+\frac{\upsilon}{c}\frac{\sigma\gamma_0^{3/2}}{\sqrt{\pi n}}\sin B_{2n,0}\right), \quad (4.23)$$

with $B_{2n,0}$ in (4.21) substituted. Finally we pass to the continuum limit, $p_0^{\mathrm{T,L}}(\omega) = \omega_B^{-1}\langle p^{\mathrm{T,L}}\rangle_{n=\omega/\omega_B}$; cf. after (4.13).

To connect to the synchrotron densities, we use the ultra-relativistic spectral functions [1],

$$\begin{aligned} L_0(\xi) &:= \frac{1}{3}\int_\xi^\infty (J_{-1/3}(x)+J_{1/3}(x))\mathrm{d}x \\ &= \frac{1}{3}\left(2-\int_0^\xi (J_{-1/3}(x)+J_{1/3}(x))\mathrm{d}x\right), \\ F_0(\xi) &:= -\frac{1}{3}\int_\xi^\infty (J_{-5/3}(x)+J_{5/3}(x))\mathrm{d}x \\ &= \frac{2}{3}(J_{-2/3}(\xi)-J_{2/3}(\xi)) - L_0(\xi), \end{aligned} \quad (4.24)$$

and their $\xi\to\infty$ limit, $(F_0, L_0)(\xi) \sim -\sqrt{2/(3\pi\xi)}\sin(\xi - \pi/4)$. We define, cf. (4.14),

$$\begin{aligned} \delta_0 &:= 3\gamma_0^3\left(\frac{1}{\gamma_0}-\arctan\frac{1}{\gamma_0}\right), \\ \xi_0(\omega) &:= \frac{2}{3\gamma_0^3}\frac{\omega}{\omega_B}\delta_0, \end{aligned} \quad (4.25)$$

with $\gamma_0(\omega)$ in (4.20). γ is kept fixed. If $\omega\to\omega_{\mathrm{b}}$, then $\gamma_0\to\infty$ and $\delta_0 = 1-(3/5)\gamma_0^{-2}+\ldots$ so that $\xi_0\to 0$. If $\omega\to 0$, then $\gamma_0\approx(\omega/\omega_{\mathrm{b}})\gamma$ and $\delta_0 = 3\gamma_0^2(1-(\pi/2)\gamma_0+\ldots)$, so that $\xi_0\approx(2/\gamma)(\omega_{\mathrm{b}}/\omega_B)$. By making use of the shortcuts δ_0 and ξ_0 in (4.25) and the $\xi\to\infty$ limit of the spectral functions (4.24), we may write the densities (4.22) and (4.23) as

$$p_0^{\mathrm{T}}(\omega) \sim \alpha_q\frac{\hbar\omega}{\sigma^2\gamma_0^2}\frac{c}{\upsilon}\left(1+\frac{\upsilon}{c}\sigma\sqrt{\delta_0}F_0(\xi_0)\right), \quad (4.26)$$

$$p_0^{\mathrm{L}}(\omega) \sim \alpha_q\frac{m_t^2c^4}{\hbar\omega\sigma^2}\frac{c}{\upsilon}\left(1-\frac{\upsilon}{c}\sigma\sqrt{\delta_0}L_0(\xi_0)\right). \quad (4.27)$$

This extends the densities (4.16) into the low-frequency band $\omega<\omega_{\mathrm{b}}$. The cross-over into the synchrotron regime is effected by substituting the exact spectral functions (4.24), rather than their $\xi\to\infty$ limit, into the densities (4.26) and (4.27); cf. Sect. 4.3.

The critical frequency of electromagnetic synchrotron radiation relates to the gyrofrequency as $\omega_{\mathrm{c}} := (3/2)\gamma^3\omega_B$ [20]. The critical tachyon frequency is $\omega_{\mathrm{ct}} := \omega_{\mathrm{b}}\sqrt{\kappa}$, where $\kappa := \omega_{\mathrm{b}}/\omega_{\mathrm{c}}$. If $\kappa\ll 1$ and $\sqrt{\kappa}\gamma\gg 1$, then $\xi_0(\omega_{\mathrm{ct}})\approx 1$, cf. (4.25), in this way ω_{ct} is defined; cf. the captions of Figs. 1–3. In [2], we denoted the critical tachyon frequency by $\omega_{\min}$. In strong magnetic fields, the transversal density admits a minimum, which is located in the vicinity of ω_{ct}.

By dropping the $\sin B_{2n,0}$-terms in (4.22) and (4.23) or, for that matter, the F_0- and L_0-terms in (4.26) and (4.27), we recover the limit of infinite orbital radius, cf. (5.1), i.e. the spectral densities of a uniformly moving charge [16],

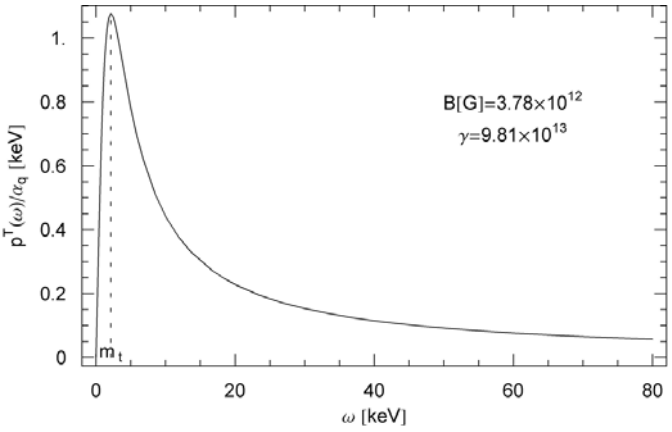

Fig. 1. Tachyonic spectral density $p_{0,\infty}^{\mathrm{T}}(\omega)$, cf. (4.33) and (4.35), in the surface field $B = 3.78\times10^{12}$ G of the Crab pulsar. The indicated electronic Lorentz factor corresponds to $k_{\max} = 10.7$, that is, an electronic orbital energy of $E = 10^{10.7}$ GeV; cf. Table 5 and after (5.3). (B and E are input) Only the low-frequency density $p_0^{\mathrm{T}}(\omega)$ is depicted, as the break frequency is at $\omega_{\mathrm{b}}\approx 2.1\times10^{14}$ keV; cf. (4.9) and (5.2). At this field strength and Lorentz factor, the longitudinal density $p_0^{\mathrm{L}}(\omega)$, cf. (4.36), is undistinguishable from the plotted transversal $p_0^{\mathrm{T}}(\omega)$ in the shown energy range. It also coincides with the ultra-relativistic synchrotron densities (4.41) and (4.42). At this resolution, the plot also coincides with that of the uniform densities $p^{\mathrm{T,L}}(\omega)$ in (4.28) and (4.29). The criterion $\Delta\gg 1$ for a continuous spectrum to arise, cf. (4.30), is amply satisfied, $\Delta\approx 4.8\times10^{12}$. The Lorentz factor considered here corresponds to the highest electronic orbital energies attained in the surface field, cf. after (5.3), with a gyrofrequency of $\omega_B\approx 4.47\times10^{-13}$ keV, cf. the beginning of Sect. 2 and (5.1), and an orbital radius of $R\approx 4.4\times10^4$ cm; cf. (5.1). The spectral peak is determined by the tachyon mass, $m_t\approx 2.15$ keV, cf. the beginning of Sects. 2 and 5, followed by an extended spectral tail with power-law decay; cf. (4.28) and (4.29). At the tachyon mass, we find $p^{\mathrm{T,L}}(m_t)/\alpha_q\approx 1.075$ keV. The plotted density is rescaled with the tachyonic fine structure constant α_q; cf. after (2.1). The critical tachyon frequency is at $\omega_{\mathrm{ct}}\approx 3.85\times10^6$ keV, cf. after (4.27) and (5.3), and $\xi_0(\omega_{\mathrm{ct}})\approx 0.9997$; cf. (4.25) and after (4.27). It is only at about this frequency that the transversal and longitudinal densities start to differ, $p^{\mathrm{T}}(\omega_{\mathrm{ct}})/\alpha_q\approx 8.3\times10^{-7}$ keV and $p^{\mathrm{L}}(\omega_{\mathrm{ct}})/\alpha_q\approx 1.2\times10^{-6}$ keV; cf. (4.35) and (4.36)

$$p^{\mathrm{T}}(\omega) \sim \frac{\alpha_q m_t^2c^4\hbar\omega}{\hbar^2\omega^2+m_t^2c^4}\left(\gamma^2-1-\frac{\hbar^2\omega^2}{m_t^2c^4}\right)\frac{1}{\gamma\sqrt{\gamma^2-1}}, \quad (4.28)$$

$$p^{\mathrm{L}}(\omega) \sim \frac{\alpha_q m_t^2c^4\hbar\omega}{\hbar^2\omega^2+m_t^2c^4}\frac{\gamma}{\sqrt{\gamma^2-1}}. \quad (4.29)$$

These densities apply in the low-frequency regime, $\omega<\omega_{\mathrm{b}}$, uniformly moving charges do not radiate above the break frequency. γ is the Lorentz factor of the source, and $\upsilon/c > m_t/(2m_{\mathrm{source}})$ is required for the classical densities to be applicable [16]. The terms containing the spectral functions in (4.26) and (4.27) stand for the curvature radiation, which shows in oscillations in the spectral densities. The condition for the $\sin B_{2n,0}$-terms in (4.22) and

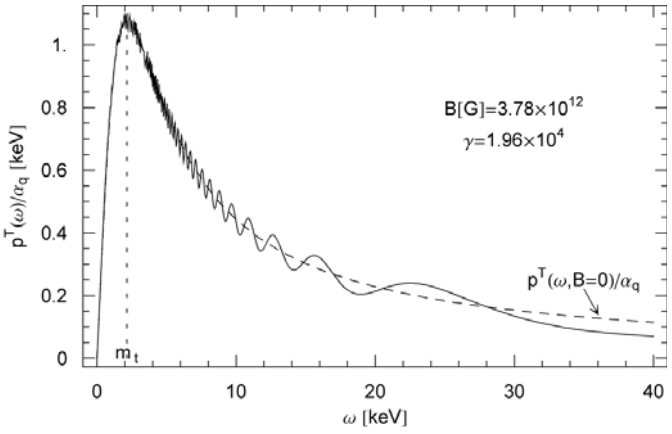

Fig. 2. Transversal tachyonic spectral density $p_0^{\mathrm{T}}(\omega)$, cf. (4.35), in the surface field of the Crab pulsar, with electronic orbital energy $E = 10\,\mathrm{GeV}$. The indicated electronic Lorentz factor is much smaller than in Fig. 1, but still in the ultra-relativistic regime, so that the plot coincides with the synchrotron density (4.41). The dashed curve is the distribution generated in straight uniform motion, $p^{\mathrm{T}}(\omega)$ in (4.28), the oscillation being superimposed by the magnetic field. Gyrofrequency and gyroradius read $\omega_{\mathrm{B}} \approx 2.24 \times 10^{-3}\,\mathrm{keV}$ and $R \approx 8.8 \times 10^{-6}\,\mathrm{cm}$. We refrain from plotting the longitudinal density $p_0^{\mathrm{L}}(\omega)$ in (4.36), which is very similar, with slightly shifted oscillations, cf. the cockscomb distributions in Figs. 3 and 4, where the Lorentz factor is lower and the difference becomes more pronounced. At the tachyon mass, we find $p^{\mathrm{T}}(m_t)/\alpha_q \approx 1.065\,\mathrm{keV}$ and $p^{\mathrm{L}}(m_t)/\alpha_q \approx 1.085\,\mathrm{keV}$. The critical frequency is $\omega_{\mathrm{ct}} \approx 54.4\,\mathrm{keV}$ so that $\xi_0(\omega_{\mathrm{ct}}) \approx 0.9991$, cf. after (4.27), $p^{\mathrm{T}}(\omega_{\mathrm{ct}})/\alpha_q \approx 0.059\,\mathrm{keV}$ and $p^{\mathrm{L}}(\omega_{\mathrm{ct}})/\alpha_q \approx 0.082\,\mathrm{keV}$. The break frequency is at $\omega_{\mathrm{b}} \approx 4.2 \times 10^4\,\mathrm{keV}$. The criterion $\Delta \gg 1$ for a continuous spectrum ist satisfied: $\Delta \approx 960$

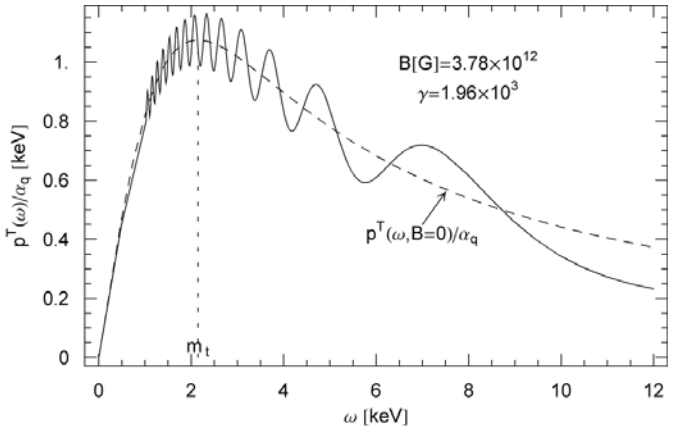

Fig. 3. Transversal tachyonic spectral density $p_0^{\mathrm{T}}(\omega)$ in (4.35), in the surface field of the Crab pulsar, with electronic orbital energy $E = 1\,\mathrm{GeV}$. The dashed curve is the distribution $p^{\mathrm{T}}(\omega)$ in (4.28), corresponding to straight uniform motion in the zero magnetic field limit, with the same Lorentz factor. Gyrofrequency and gyroradius read $\omega_{\mathrm{B}} \approx 0.0224\,\mathrm{keV}$ and $R \approx 8.8 \times 10^{-7}\,\mathrm{cm}$. The spectral peak is still located at about the tachyon mass, $p^{\mathrm{T}}(m_t)/\alpha_q \approx 1.039\,\mathrm{keV}$. Break and critical frequency read $\omega_{\mathrm{b}} \approx 4.2 \times 10^3\,\mathrm{keV}$ and $\omega_{\mathrm{ct}} \approx 17.2\,\mathrm{keV}$, respectively. We note $\xi_0(\omega_{\mathrm{ct}}) \approx 0.991$, cf. after (4.27), and $p^{\mathrm{T}}(\omega_{\mathrm{ct}})/\alpha_q \approx 0.18\,\mathrm{keV}$. The criterion for a continuous spectrum is still satisfied, $\Delta \approx 96$; discrete lines will finally emerge out of the oscillations

(4.23) to be negligible is apparently $(v/c)^2\sigma^2\gamma_0^3 \ll \omega/\omega_B$. If $\omega \ll \omega_{\mathrm{b}}$, we have $\gamma_0 \sim (c/v)\hbar\omega/(m_t c^2)$, so that the mentioned condition is tantamount to

$$\Delta := \frac{v}{c}\frac{m_t c^2}{\hbar\omega_B} \gg 1. \tag{4.30}$$

This is just the opposite limit discussed in Sect. 3 and readily understood. The bulk of the spectral densities is roughly located at $(v/c)m_t c^2$. For the continuum approximation to be applicable to the frequencies $n\omega_B$, the frequency of the spectral peak must be much larger than ω_B.

4.3 Extension of the ultra-relativistic spectral densities into the mildly relativistic and non-relativistic regimes

The spectral functions (4.15) and (4.24) can be expressed by Airy integrals [1, 19],

$$F_\infty(\xi) = -\frac{2}{z}\mathrm{Ai}'(z) - \int_z^\infty \mathrm{Ai}(x)\mathrm{d}x,$$
$$L_\infty(\xi) = \int_z^\infty \mathrm{Ai}(x)\mathrm{d}x, \tag{4.31}$$

$$F_0(\xi) = -\frac{2}{z}\mathrm{Ai}'(-z) - 1 + \int_{-z}^\infty \mathrm{Ai}(x)\mathrm{d}x,$$
$$L_0(\xi) = 1 - \int_{-z}^\infty \mathrm{Ai}(x)\mathrm{d}x,$$

where $z := (3\xi/2)^{2/3}$. We also mention the $\xi \to 0$ limits

$$F_\infty(\xi) = \frac{4}{3}\frac{\xi^{-2/3}}{2^{1/3}\Gamma(1/3)} - \frac{1}{3} + \ldots,$$
$$L_\infty(\xi) = \frac{1}{3} - \frac{\xi^{2/3}}{2^{2/3}\Gamma(2/3)} + \ldots,$$
$$F_0(\xi) = \frac{4}{3}\frac{\xi^{-2/3}}{2^{1/3}\Gamma(1/3)} - \frac{2}{3} + \ldots, \tag{4.32}$$
$$L_0(\xi) = \frac{2}{3} - \frac{\xi^{2/3}}{2^{2/3}\Gamma(2/3)} + \ldots,$$

all up to terms of $O(\xi^{4/3})$. The high-frequency densities (4.16) thus read

$$p_\infty^{\mathrm{T}}(\omega) = \alpha_q\hbar\omega\frac{\sqrt{\delta_\infty}}{\sigma\gamma_\infty^2}\left(-\frac{2}{z_\infty}\mathrm{Ai}'(z_\infty) - \int_{z_\infty}^\infty \mathrm{Ai}(x)\mathrm{d}x\right), \tag{4.33}$$

$$p_\infty^{\mathrm{L}}(\omega) = \alpha_q\frac{m_t^2c^4}{\hbar\omega}\frac{\sqrt{\delta_\infty}}{\sigma}\int_{z_\infty}^\infty \mathrm{Ai}(x)\mathrm{d}x, \tag{4.34}$$

where $z_\infty := (3\xi_\infty/2)^{2/3}$; cf. (4.8), (4.11), and (4.14).

The Airy representation of the transversal density (4.26) in the low-frequency regime is

$$p_0^{\mathrm{T}}(\omega) = \alpha_q\hbar\omega\frac{\sqrt{\delta_0}}{\sigma\gamma_0^2}\left(\frac{2}{z_0}\mathrm{Ai}'(z_0)+\int_{z_0}^{\infty}\mathrm{Ai}(x)\mathrm{d}x\right) + q_0^{\mathrm{T}}(\omega),$$
$$q_0^{\mathrm{T}}(\omega) := \alpha_q\hbar\omega\frac{1}{\sigma^2\gamma_0^2}\frac{c}{\upsilon}\left(1-\frac{\upsilon}{c}\sigma\sqrt{\delta_0}\right), \qquad (4.35)$$

and the longitudinal low-frequency distribution (4.27) reads

$$p_0^{\mathrm{L}}(\omega) = \alpha_q\frac{m_t^2c^4}{\hbar\omega}\frac{\sqrt{\delta_0}}{\sigma}\int_{z_0}^{\infty}\mathrm{Ai}(x)\mathrm{d}x + q_0^{\mathrm{L}}(\omega),$$
$$q_0^{\mathrm{L}}(\omega) := \alpha_q\frac{m_t^2c^4}{\hbar\omega}\frac{1}{\sigma^2}\frac{c}{\upsilon}\left(1-\frac{\upsilon}{c}\sigma\sqrt{\delta_0}\right), \qquad (4.36)$$

where $z_0 := -(3\xi_0/2)^{2/3}$; cf. (4.8), (4.20), and (4.25) (z_0 is defined negative). More explicitly,

$$z_{\infty,0} = (\omega/\omega_B)^{2/3}\left(1-\frac{\omega_{\mathrm{b}}^2}{\omega^2}\right)\frac{\delta_{\infty,0}^{2/3}}{\gamma^2}. \qquad (4.37)$$

The notation is explained in the preceding subsections. At the break frequency, the high- and low-frequency densities join continuously, $p_\infty^{\mathrm{T,L}}(\omega_{\mathrm{b}}) = p_0^{\mathrm{T,L}}(\omega_{\mathrm{b}})$. In fact, $p_0^{\mathrm{T,L}}(\omega) - q_0^{\mathrm{T,L}}(\omega)$ is the analytic continuation of $p_\infty^{\mathrm{T,L}}(\omega)$. (If we substitute $\gamma_0 \to \mathrm{i}\gamma_\infty$, then $\delta_0 \to \delta_\infty$, $\xi_0 \to \mathrm{i}^{-3}\xi_\infty$, better not to simplify, and $z_0 \to z_\infty$.) The $\varepsilon := (\omega-\omega_{\mathrm{b}})/\omega_{\mathrm{b}}$-expansion of $q_0^{\mathrm{T,L}}$ gives in lowest order

$$q_0^{\mathrm{T}}(\omega) \sim -\frac{4}{5}\alpha_q m_t c^2\frac{\gamma^2-1}{\gamma^5}\varepsilon^2,$$
$$q_0^{\mathrm{L}}(\omega) \sim \frac{2}{5}\alpha_q m_t c^2\frac{\varepsilon}{\gamma^3}, \qquad (4.38)$$

where we used $\gamma_0^{-2} \sim -(2/\gamma^2)\varepsilon$. There is no counterpart to the $q_0^{\mathrm{T,L}}$-terms in the upper frequency range. Contrary to the longitudinal density, the transversal density is thus smooth, as the first derivatives of p_∞^{T} and p_0^{T} coincide at ω_{b}.

To cope with the slow convergence, we substitute

$$\int_{z_\infty}^{\infty}\mathrm{Ai}(x)\mathrm{d}x = \frac{1}{3}-\int_0^{z_\infty}\mathrm{Ai}(x)\mathrm{d}x,$$
$$\int_{z_0}^{\infty}\mathrm{Ai}(x)\mathrm{d}x = \frac{1}{3}+\int_0^{-z_0}\mathrm{Ai}(-x)\mathrm{d}x \qquad (4.39)$$

into the densities (4.33)–(4.36), and use, for large $z_{\infty,0}$,

$$\int_0^z\mathrm{Ai}(x)\mathrm{d}x \sim \frac{1}{3}-\frac{1}{2\sqrt{\pi}z^{3/4}}\exp\left(-\frac{2}{3}z^{3/2}\right), \qquad (4.40)$$
$$\int_0^z\mathrm{Ai}(-x)\mathrm{d}x \sim \frac{2}{3}+\frac{1}{\sqrt{\pi}z^{3/4}}\sin\left(\frac{2}{3}z^{3/2}-\frac{\pi}{4}\right).$$

This is particularly efficient in the low-frequency regime (4.35) and (4.36). The plots in Figs. 1–14 give an overview

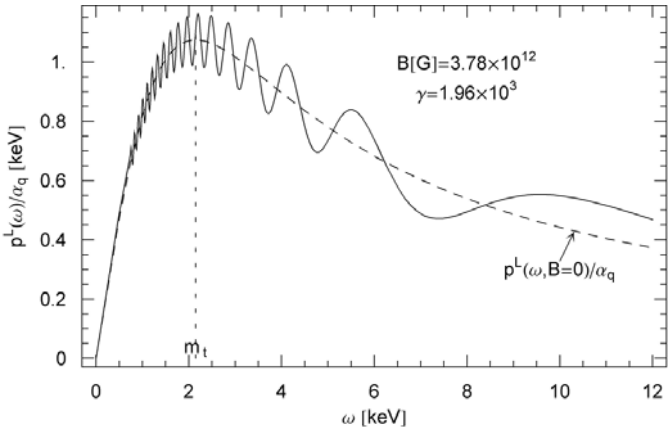

Fig. 4. Longitudinal spectral density $p_0^{\mathrm{L}}(\omega)$, cf. (4.36), with parameters as in Fig. 3. The dashed curve is the uniform distribution $p^{\mathrm{L}}(\omega)$ in (4.29), recovered in the limit of infinite orbital radius or vanishing field strength. At this Lorentz factor, the longitudinal oscillations become noticeably different from the transversal cockscomb in Fig. 3. At the tachyon mass, $p^{\mathrm{L}}(m_t)/\alpha_q \approx 1.11\,\mathrm{keV}$, and $p^{\mathrm{L}}(\omega_{\mathrm{ct}})/\alpha_q \approx 0.25\,\mathrm{keV}$ at the critical frequency. The plots in Figs. 3 and 4 still coincide with the transversal and longitudinal synchrotron densities (4.41) and (4.42), respectively

of the transversal and longitudinal densities (4.33)–(4.36), illustrating the different regimes determined by the field strength and the Lorentz factor. In Figs. 1–4, we consider electrons cycling in the surface magnetic field of the Crab pulsar, with ultra-relativistic Lorentz factors. In Figs. 5–14, we study the tachyonic cyclotron regime in the light cylinder field of this pulsar, in particular the cross-over from relativistic to non-relativistic electronic orbital energy. We refer to the figure captions for further discussion; the parameters invoked in the captions to characterize the shape of the densities are summarized in Sect. 5.

We finally relate the densities derived here to the ultra-relativistic synchrotron densities, obtained as the leading order in a $1/\gamma$-expansion [1],

$$p^{\mathrm{T}}(\omega) = \frac{\alpha_q m_t^2c^4\hbar\omega}{\hbar^2\omega^2+m_t^2c^4}\left(1-\frac{\omega^2}{\omega_{\mathrm{sync}}^2}\right) \times\left(\frac{2}{\eta}\mathrm{Ai}'(\eta)+\int_\eta^\infty\mathrm{Ai}(x)\mathrm{d}x\right), \qquad (4.41)$$
$$p^{\mathrm{L}}(\omega) = \frac{\alpha_q m_t^2c^4\hbar\omega}{\hbar^2\omega^2+m_t^2c^4}\int_\eta^\infty\mathrm{Ai}(x)\mathrm{d}x, \qquad (4.42)$$
$$\eta(\omega) := (\omega/\omega_B)^{2/3}\left(1-\frac{\omega_{\mathrm{sync}}^2}{\omega^2}\right)\frac{1}{\gamma^2},$$
$$\omega_{\mathrm{sync}} := m_tc^2\gamma/\hbar. \qquad (4.43)$$

First, $\delta_{\infty,0} \to 1$ if $\gamma \to \infty$, cf. after (4.14) and (4.25), and $\omega_{\mathrm{b}} \sim \omega_{\mathrm{sync}}$; cf. (4.9). Thus we can identify $z_{\infty,0}$ in (4.37) with $\eta(\omega)$ defined in (4.43). In the upper frequency range ($\omega > \omega_{\mathrm{b}}$), we therefore have $m_tc^2/(\hbar\omega) < 1/\gamma$, and we can drop such terms. Thus the densities

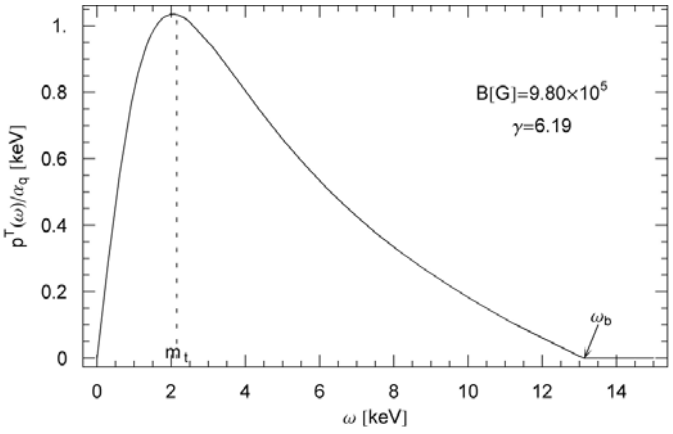

Fig. 5. Transversal tachyonic spectral density $p^{\mathrm{T}}_{0,\infty}(\omega)$, cf. (4.33) and (4.35), in the light cylinder field of the Crab pulsar; cf. Table 6. In Figs. 5–14, we consider the mildly relativistic and non-relativistic cyclotron regime. Higher Lorentz factors (within the permissible range defined by $k^{(\mathrm{lc})}_{\max} = 4.15$ in Tables 6 and 8) quickly wipe out the oscillations induced by the magnetic field, $B = 9.80 \times 10^5$ G, so that we are left with the uniform distributions in (4.28) and (4.29) like in Fig. 1. Even at a Lorentz factor this low, $\gamma = 6.19$, there are no oscillations visible at the scale of this figure, but they get apparent along the spectral slope in the close-up of Fig. 6. Depicted are $p^{\mathrm{T}}_0(\omega)$ in (4.35) for $\omega < \omega_{\mathrm{b}}$ and $p^{\mathrm{T}}_\infty(\omega)$ for $\omega > \omega_{\mathrm{b}}$, with the break frequency at $\omega_{\mathrm{b}} \approx 13.1\,\mathrm{keV}$. In the latter case, the exponential decay is so rapid, that $p^{\mathrm{T}}_\infty(\omega)$ is just zero; even in the close-up of Fig. 6 the slope is barely visible. The electronic orbital energy is $E = 10^{-2.5}\,\mathrm{GeV}$ (E and B are input), gyrofrequency, gyroradius, and orbital speed read $\omega_{\mathrm{B}} \approx 1.83 \times 10^{-6}\,\mathrm{keV}$, $R \approx 0.011\,\mathrm{cm}$, and $v/c \approx 0.987$, respectively; cf. Sect. 5. The criterion for continuum radiation is satisfied, $\Delta \approx 1.2 \times 10^6$; cf. (4.30). $p^{\mathrm{T}}(m_t)/\alpha_q \approx 1.03\,\mathrm{keV}$ at the spectral peak, and $p^{\mathrm{T}}(\omega_{\mathrm{b}})/\alpha_q \approx 1.8 \times 10^{-4}\,\mathrm{keV}$ at the break frequency. The critical frequency ω_{ct} lies above the break frequency, cf. Table 6, in contrast to the previous ultra-relativistic high magnetic field examples. The parameters stated here apply to Figs. 5–8

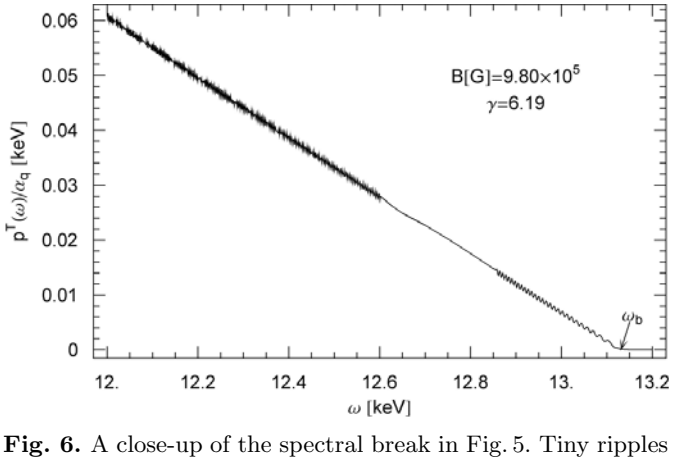

Fig. 6. A close-up of the spectral break in Fig. 5. Tiny ripples emerge due to the magnetic field. By zooming in further, we find a fine structure similar to that of Fig. 10. The oscillations vanish in the zero magnetic field limit, for uniform motion as defined by $p^{\mathrm{T}}(\omega)$ in (4.28)

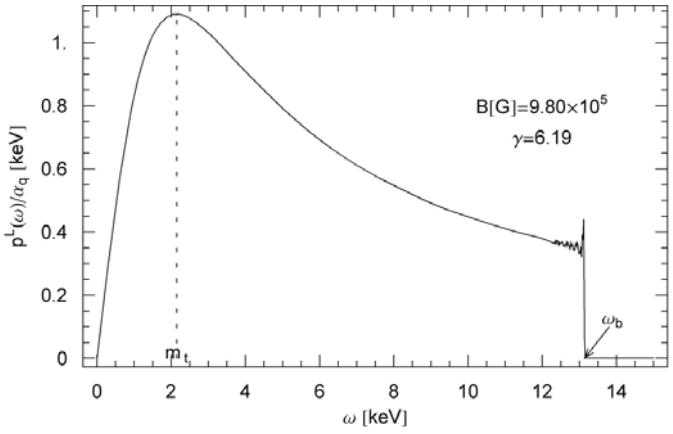

Fig. 7. The longitudinal spectral density $p^{\mathrm{L}}_{0,\infty}(\omega)$, cf. (4.34) and (4.36), with parameters as in Fig. 5. At the spectral peak, we find $p^{\mathrm{L}}(m_t)/\alpha_q \approx 1.09\,\mathrm{keV}$. There is no discontinuity at the break frequency ω_{b}, just oscillations followed by exponential decay; cf. the close-up in Fig. 8

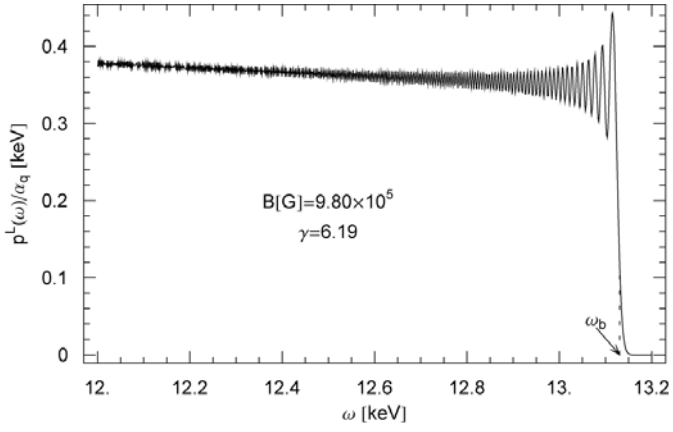

Fig. 8. A close-up of the spectral break in Fig. 7 shows rapid oscillations followed by exponential decay of $p^{\mathrm{L}}_\infty(\omega)$ right at the spectral break. At the break frequency, $p^{\mathrm{L}}(\omega_{\mathrm{b}})/\alpha_q \approx 0.116\,\mathrm{keV}$. Also compare Fig. 12

(4.33) and (4.34) coincide with (4.41) and (4.42), respectively. We turn to the low-frequency regime. If $\omega \ll \omega_{\mathrm{b}}$, then $\gamma_0 \sim \hbar\omega/(m_t c^2)$. There are two cases to consider. If $m_t c^2/(\hbar\omega) \ll 1$, then the $q^{\mathrm{T,L}}_0(\omega)$-terms in the low-frequency densities (4.35) and (4.36) can be dropped. (σ can be expanded in the indicated parameter, and $\delta_0 \sim 1$, cf. after (4.25), so that the $q^{\mathrm{T,L}}_0(\omega)$-terms are by a factor $(m_t c^2/(\hbar\omega))^2$ smaller than the terms containing the Airy functions in (4.35) and (4.36).) This implies coincidence in the regime $m_t c^2/\hbar \ll \omega \ll \omega_{\mathrm{b}}$. The second case, $m_t c^2/(\hbar\omega) \gg 1$, means $\xi_0 \approx 2m_t c^2/(\hbar\omega_B)$, cf. after (4.25), which implies $\xi_0 \gg 1$; cf. (4.30). Therefore, we may replace in (4.26) and (4.27) the spectral functions by their asymptotic limits, so that we end up with the Debye asymptotics (4.22) and (4.23). The conditions $\omega \ll \omega_{\mathrm{b}}$ and $m_t c^2/(\hbar\omega) \gg 1$ are sufficient to neglect the $\sin B_{2n,0}$-terms in (4.22) and (4.23), as pointed out after (4.29). Hence, in the frequency range $\omega \ll m_t c^2/\hbar$, we are left with the spectral densities (4.28) and (4.29) of freely

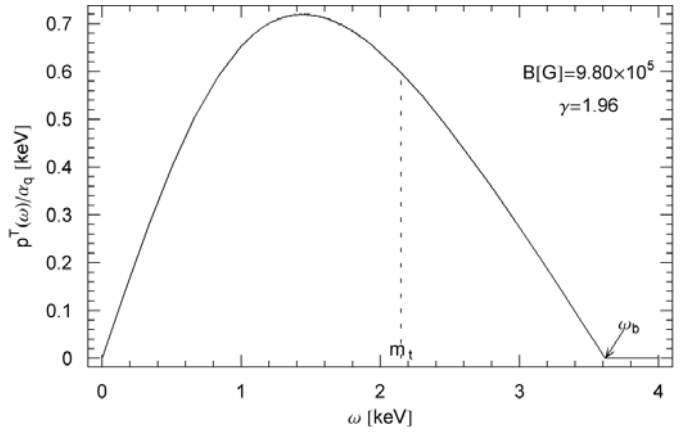

Fig. 9. Transversal tachyonic spectral density $p^{\mathrm{T}}_{0,\infty}(\omega)$, cf. (4.33) and (4.35), in the light cylinder field of the Crab pulsar. The Lorentz factor is further decreased as compared to Figs. 5–8. The electronic orbital energy is $E = 1\,\mathrm{MeV}$, gyrofrequency and gyroradius read $\omega_{\mathrm{B}} \approx 5.80 \times 10^{-6}\,\mathrm{keV}$ and $R \approx 2.9 \times 10^{-3}\,\mathrm{cm}$, respectively; the orbital speed is $v/c \approx 0.860$. The criterion for continuum radiation is satisfied, $\Delta \approx 3.2 \times 10^5$, as suggested by the absence of visible modulations. In the surface field, cf. Figs. 1–4, we have not considered such small Lorentz factors, as this would have been in conflict with the criterion for a continuous spectrum to arise, $\Delta \gg 1$. The break frequency is at $\omega_{\mathrm{b}} \approx 3.62\,\mathrm{keV}$, and $p^{\mathrm{T}}(\omega_{\mathrm{b}})/\alpha_q \approx 2.2 \times 10^{-4}\,\mathrm{keV}$. The spectral peak is now shifted away from the tachyon mass. A further decrease of the Lorentz factor into the non-relativistic regime is admissible and can drive the break frequency below the tachyon mass; cf. Figs. 13 and 14. In the given resolution, the plot coincides with the uniform density $p^{\mathrm{T}}(\omega)$ in (4.28). A close-up of the density at the spectral break is given in Fig. 10. The parameters stated here apply to Figs. 9–12

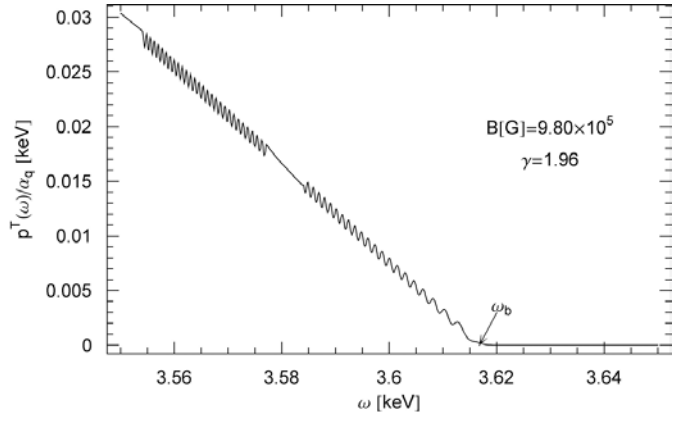

Fig. 10. Close-up of the spectral break in Fig. 9. The ripples are the only manifestation of the magnetic field, the finite orbital radius that is, and are smoothed out in the zero magnetic field limit. A lesser resolution results in a pattern similar to Fig. 6

moving sources. A similar reasoning applies to the ultra-relativistic densities (4.41) and (4.42) to the same effect, the curvature radiation being negligible in this regime. In this way, we have demonstrated equivalence of the ultra-relativistic synchrotron densities (4.41) and (4.42) with

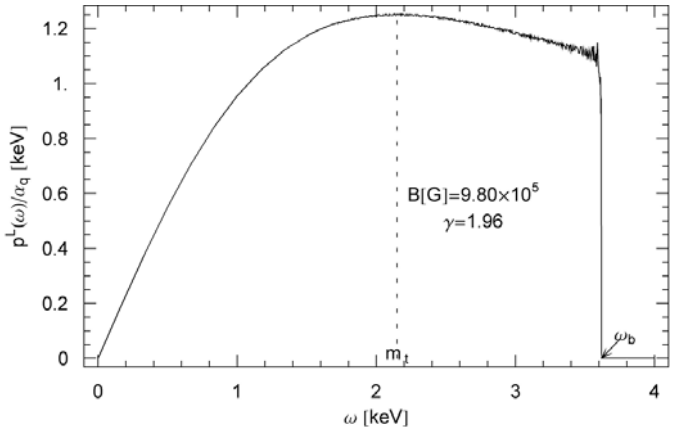

Fig. 11. Longitudinal cyclotron density $p^{\mathrm{L}}_{0,\infty}(\omega)$, cf. (4.34) and (4.36), with parameters as in Fig. 9. The longitudinal spectral maximum is still at the tachyon mass, $p^{\mathrm{L}}(m_t)/\alpha_q \approx 1.25\,\mathrm{keV}$. The spectral break at ω_{b} is continuous; cf. the close-up in Fig. 12. Apart from tiny modulations, the plot coincides with the uniform longitudinal density $p^{\mathrm{L}}(\omega)$ in (4.29)

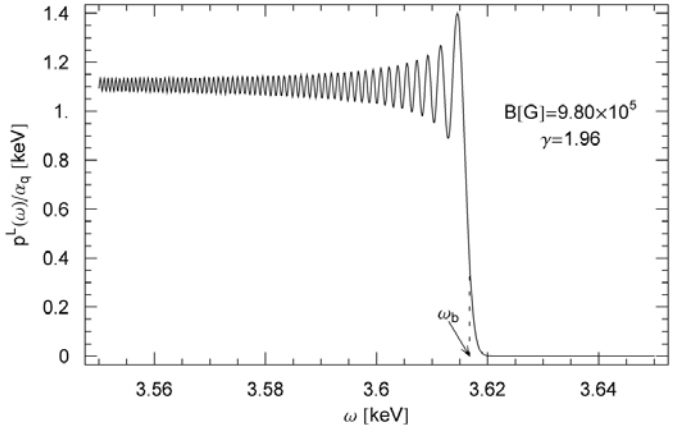

Fig. 12. Close-up of the longitudinal density in Fig. 11. At the spectral break, $p^{\mathrm{L}}(\omega_{\mathrm{b}})/\alpha_q \approx 0.37\,\mathrm{keV}$. We find modulations similar to Fig. 8 along the spectral slope

the $\gamma \gg 1$ asymptotics of the densities (4.33)–(4.36). The latter are applicable irrespectively of the magnitude of the Lorentz factor, they extend the synchrotron densities into the weakly relativistic regime, and even into the non-relativistic cyclotron regime, provided condition (4.30) for continuum radiation is met.

5 Tachyonic cyclotron and synchrotron radiation from rotation-powered pulsars

We give a phenomenological discussion of the tachyonic spectral densities derived in the previous section, studying electrons and protons orbiting in the surface and light cylinder fields of γ-ray and millisecond pulsars. The energy of the orbiting source particles and the magnetic field strength are taken as input parameters. Most of the notation has already been introduced at the beginning

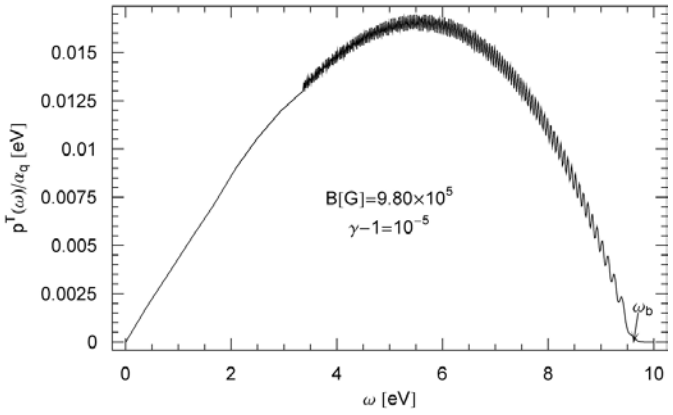

Fig. 13. The continuous non-relativistic cyclotron regime. The transversal tachyonic spectral density $p^{\rm T}_{0,\infty}(\omega)$, cf. (4.33) and (4.35), is plotted in the light cylinder field of the Crab pulsar, at a gyration energy of $E - m_{\rm e}c^2 \approx 5.11\,{\rm eV}$ (input $\gamma - 1 = 10^{-5}$ and $B = 9.80 \times 10^5\,{\rm G}$). The electronic orbital speed is $v/c \approx 4.47 \times 10^{-3}$, gyrofrequency and gyroradius read $\omega_{\rm B} \approx 0.01135\,{\rm eV}$ and $R \approx 7.8 \times 10^{-6}\,{\rm cm}$. The energy scale in Figs. 13 and 14 is eV; the break frequency, $\omega_{\rm b} \approx 9.615\,{\rm eV}$, lies far below the tachyon mass, and $p^{\rm T}(\omega_{\rm b})/\alpha_q \approx 2.49 \times 10^{-4}\,{\rm eV}$. The criterion for a continuous spectrum is met, $\Delta \approx 847$; cf. (4.30). Comparing to the previous figures, the smaller Δ the larger are the modulations, which provide the onset for discrete line spectra; cf. Sect. 3. The magnetic field is manifested in the oscillating fine structure. If smoothed out, the plot coincides with the uniform density $p^{\rm T}(\omega)$ in (4.28)

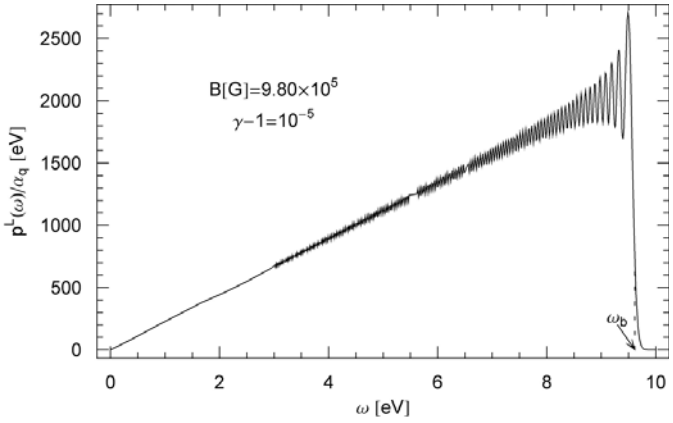

Fig. 14. Longitudinal tachyonic spectral density $p^{\rm L}_{0,\infty}(\omega)$ in (4.34) and (4.36), with parameters as in Fig. 13. The energy scales of the longitudinal density and its transversal counterpart in Fig. 13 differ by some five orders at the spectral peaks. The transversal power radiated in the non-relativistic cyclotron regime is thus negligible as compared to the longitudinal continuum radiation. At the spectral break, $p^{\rm L}(\omega_{\rm b})/\alpha_q \approx 717\,{\rm eV}$. The spectral maximum is reached close to the spectral break, immediately followed by exponential decay. The oscillations induced by the magnetic field are absent in the uniform density $p^{\rm L}(\omega)$ in (4.29), which is very nearly linear up to the spectral break and then drops to zero

of Sects. 2 and 4. We summarize it here in a dimensionless way convenient for compiling the tables and setting the scales of the figures in Sect. 4. The tachyon mass is 2.15 keV, the tachyon/electron and tachyon/proton mass ratios are $m_t/m_e \approx 4.21 \times 10^{-3}$ and $m_t/m_p \approx 2.29 \times 10^{-6}$, respectively. The energy $E = mc^2\gamma$ of the orbiting source particle is parametrized as $E\,[{\rm GeV}] = 10^k$, for electrons and protons alike, so that the respective Lorentz factors are $\gamma^{(e)} \approx 1.957 \times 10^{3+k}$ and $\gamma^{(p)} \approx 1.066 \times 10^k$. Apart from the tachyon mass, there are four other energy scales defined by the gyrofrequency ω_B, cf. the beginning of Sect. 2, the tachyonic break frequency $\omega_{\rm b}$, cf. (4.9), the critical photon frequency $\omega_{\rm c}$ and the critical tachyon frequency $\omega_{\rm ct}$; cf. after (4.27).

Gyrofrequency and gyroradius scale as, cf. (2.1),

$$\omega_B\,[{\rm keV}] \approx 5.916 \times 10^{-15} B\,[{\rm G}]/E\,[{\rm GeV}], \qquad (5.1)$$
$$R = \hat{R}v/c,$$
$$\hat{R}\,[{\rm cm}] \approx 1.973 \times 10^{-8}/\omega_B\,[{\rm keV}].$$

Contrary to Sects. 2 and 3, we use capital R for the orbital radius and write ω for $\hbar\omega$. Quantities with a hat indicate that a power of v/c has been split off, so that they scale with E and B like in (5.1). If the source particle is ultra-relativistic, we can put $v/c \approx 1$. At low energy, we have to rescale the quantities listed in the tables with the appropriate power of $v/c = \sqrt{\gamma^{(e,p)2} - 1}/\gamma^{(e,p)}$. There is no electromagnetic counterpart to the tachyonic cyclotron densities, that is, to the superluminal continuum radiation from sources orbiting at low energy. Electromagnetic cyclotron emission, the non-relativistic limit of synchrotron radiation, always gives rise to line spectra, similarly as discussed in Sect. 3. Finally, there is a lower bound on the Lorentz factor of the source particle, $\gamma^{(e,p)} > \sqrt{1 + m_t^2/(4m_{e,p}^2)}$, for the classical theory to be applicable [16], but this is not very stringent, $\gamma^{(e)} - 1 > 2.2 \times 10^{-6}$ and $\gamma^{(p)} - 1 > 6.5 \times 10^{-13}$, so that a lower bound on the energy $E\,[{\rm GeV}] = 10^k$ of the radiating source is still defined by the particle mass, $k^{(e)}_{\rm min} \approx -3.29$, and $k^{(p)}_{\rm min} \approx -0.027$ for protons; cf. Fig. 13.

The tachyonic break frequency scales as $\omega_{\rm b} = \hat{\omega}_{\rm b}v/c$, where $\hat{\omega}_{\rm b} = m_t c^2\gamma$, cf. (4.9), so that

$$\hat{\omega}^{(e)}_{\rm b}\,[{\rm keV}] \approx 4.21 \times 10^3 E\,[{\rm GeV}],$$
$$\hat{\omega}^{(p)}_{\rm b}\,[{\rm keV}] \approx 2.29 E\,[{\rm GeV}], \qquad (5.2)$$

for electrons and protons, respectively. The critical frequencies were introduced after (4.27). The critical photon frequency reads $\omega^{(e,p)}_{\rm c}\,[{\rm keV}] = (3/2)\gamma^{(e,p)3}\omega_B\,[{\rm keV}]$, for electronic/protonic sources. It does not scale with v/c, and we may substitute ω_B, cf. (5.1), and $\gamma^{(e)} \approx 1957E\,[{\rm GeV}]$ or $\gamma^{(p)} \approx 1.066E\,[{\rm GeV}]$. The ratio $\kappa = \omega_{\rm b}/\omega_{\rm c}$ of break frequency and critical photon frequency scales as $\kappa = \hat{\kappa}v/c$, where $\hat{\kappa} := \hat{\omega}_{\rm b}/\omega_{\rm c}$. The critical tachyon frequency is $\omega_{\rm ct} = \sqrt{\kappa}\omega_{\rm b}$ and scales as $\omega_{\rm ct} = (v/c)^{3/2}\hat{\omega}_{\rm ct}$, where $\hat{\omega}_{\rm ct} := \hat{\omega}^{3/2}_{\rm b}/\omega^{1/2}_{\rm c}$. We may write this more explicitly as $\hbar\hat{\omega}_{\rm ct} = \sqrt{2(m_t c^2)^3 E/(3\hbar ceB)}$ or, in dimensionless quantities,

$$\hat{\omega}_{\rm ct}\,[{\rm keV}] \approx 3.347 \times 10^7 E^{1/2}\,[{\rm GeV}]/B^{1/2}\,[{\rm G}], \qquad (5.3)$$

Table 5. Radiation from electrons orbiting in the surface fields: parameters determining the spectral densities. Surface field B (input, taken from [32]), gyrofrequency $\omega_{\rm B}$; cf. (5.1). k labels the electronic or protonic source energy, E (GeV) $= 10^k$ (input). Critical photon frequency $\omega_{\rm c}^{(e)}$ for electronic source particles; cf. after (5.2). Critical tachyon frequency $\hat\omega_{\rm ct}$, independent of the mass of the source particle; cf. (5.3). In the case of mildly relativistic particles, $\hat\omega_{\rm ct}$ has to be rescaled, $\omega_{\rm ct} = (v/c)^{3/2}\hat\omega_{\rm ct}$. Here, $v/c = \sqrt{\gamma^2-1}/\gamma$ is the speed of the orbiting source, where $\gamma \approx 1.957\times 10^{3+k}$ for electrons. Gyroradius $\hat R$, cf. (5.1), or $R = \hat R v/c$, if rescaled. $\hat\kappa^{(e)}$ denotes the ratio $\hat\omega_{\rm b}^{(e)}/\omega_{\rm c}^{(e)}$ of tachyonic break energy and critical photon energy, rescaled as $\kappa = \hat\kappa v/c$. The tachyonic break frequency is parametrized as $\hat\omega_{\rm b}^{(e)}({\rm keV}) \approx 4.21\times 10^{3+k}$, $\omega_{\rm b} = \hat\omega_{\rm b} v/c$; cf. (5.2). The energy $E\,({\rm GeV}) = 10^k$ of the orbiting electrons ranges between $k_{\rm min}^{(e)} \approx -3.29$ and $k_{\rm max}$. The latter is determined by equating the critical tachyon frequency with the observed cutoff in the γ-ray spectrum; cf. Sect. 5. $k_{\rm max}$ applies to protonic sources in the surface fields as well. The high-magnetic field pulsar PSR B1509–58 has a very low cutoff energy of 10 MeV. The Crab pulsar (PSR B0531+21), PSR B1706–44, and PSR B1951+32 admit γ-ray spectra extending up to 20 GeV. PSR J0218+4232 (at 5.85 kpc) is the only millisecond pulsar marginally detected in γ-rays

	B (G)	$\omega_{\rm B}$ (keV)	$\omega_{\rm c}^{(e)}$ (keV)	$\hat\omega_{\rm ct}$ (keV)	$\hat R$ (cm)	$\hat\kappa^{(e)}$	$k_{\rm max}$
γ-ray pulsars							
B1509–58	1.54×10^{13}	$9.11\times 10^{-2-k}$	$1.02\times 10^{9+2k}$	$8.53\times 10^{k/2}$	$2.17\times 10^{-7+k}$	$4.10\times 10^{-6-k}$	6.14
Crab	3.78×10^{12}	$2.24\times 10^{-2-k}$	$2.51\times 10^{8+2k}$	$1.72\times 10^{1+k/2}$	$8.83\times 10^{-7+k}$	$1.67\times 10^{-5-k}$	10.7
B1706–44	3.12×10^{12}	$1.85\times 10^{-2-k}$	$2.08\times 10^{8+2k}$	$1.89\times 10^{1+k/2}$	$1.07\times 10^{-6+k}$	$2.03\times 10^{-5-k}$	12.0
B1951+32	4.86×10^{11}	$2.88\times 10^{-3-k}$	$3.23\times 10^{7+2k}$	$4.80\times 10^{1+k/2}$	$6.86\times 10^{-6+k}$	$1.30\times 10^{-4-k}$	11.2
ms-pulsar							
J0218+4232	4.29×10^{8}	$2.54\times 10^{-6-k}$	$2.85\times 10^{4+2k}$	$1.62\times 10^{3+k/2}$	$7.78\times 10^{-3+k}$	$1.47\times 10^{-1-k}$	5.58

Table 6. Parameters for cyclotron and synchrotron radiation from electrons orbiting in the light cylinder field $B^{\rm (lc)}$ (input; cf. [32]). The parameters are defined in the caption of Table 5. The energy of the cycling electrons is again parametrized by $E\,({\rm GeV}) = 10^k$, with $k_{\rm min}^{(e)} \approx -3.29$, and the tachyonic break energy reads $\hat\omega_{\rm b}^{(e)}\,({\rm keV}) \approx 4.21\times 10^{3+k}$, like in the surface fields

	$B^{\rm (lc)}$ (G)	$\omega_{\rm B}^{\rm (lc)}$ (keV)	$\omega_{\rm c}^{(e,{\rm lc})}$ (keV)	$\hat\omega_{\rm ct}^{\rm (lc)}$ (keV)	$\hat R^{\rm (lc)}$ (cm)	$\hat\kappa^{(e,{\rm lc})}$	$k_{\rm max}^{\rm (lc)}$
γ-ray pulsars							
B1509–58	4.22×10^{4}	$2.50\times 10^{-10-k}$	2.81×10^{2k}	$1.63\times 10^{5+k/2}$	$7.90\times 10^{1+k}$	$1.50\times 10^{3-k}$	−2.42
Crab	9.80×10^{5}	$5.80\times 10^{-9-k}$	$6.52\times 10^{1+2k}$	$3.38\times 10^{4+k/2}$	3.40×10^{k}	$6.44\times 10^{1-k}$	4.15
B1706–44	2.72×10^{4}	$1.61\times 10^{-10-k}$	1.81×10^{2k}	$2.03\times 10^{5+k/2}$	$1.23\times 10^{2+k}$	$2.33\times 10^{3-k}$	3.99
B1951+32	7.38×10^{4}	$4.37\times 10^{-10-k}$	4.91×10^{2k}	$1.23\times 10^{5+k/2}$	$4.52\times 10^{1+k}$	$8.57\times 10^{2-k}$	4.42
ms-pulsar							
J0218+4232	3.21×10^{5}	$1.90\times 10^{-9-k}$	$2.14\times 10^{1+2k}$	$5.91\times 10^{4+k/2}$	$1.04\times 10^{1+k}$	$1.97\times 10^{2-k}$	2.46

for electronic and protonic sources alike. In contrast, $\hat\kappa$, $\hat\omega_{\rm b}$ and $\hat\omega_{\rm c}$ depend on the mass of the source particle, so that we write these quantities with superscripts (e,p) in the tables. The gyrofrequency ω_B, the rescaled gyroradius $\hat R$, cf. (5.1), and the rescaled critical tachyon frequency $\hat\omega_{\rm ct}$ do not depend on the mass if parametrized by E and B.

The upper edge $E_{\rm max}\,[{\rm GeV}] = 10^{k_{\rm max}}$ of the source energy, that is, the highest energy attained by electrons and protons orbiting in the surface field, is inferred by equating the critical frequency $\omega_{\rm ct}(E)$ in (5.3) with the upper cutoff of the observed γ-ray spectrum. The cutoffs quoted below are in fact only lower bounds, and so is $k_{\rm max}$ listed in Table 5, a lower bound on the maximal orbital energy attained. The cutoff energy of the Crab pulsar is taken as 4 GeV [21], the γ-ray spectra of PSR B1706–44 and PSR B1951+32 extend up to at least 20 GeV [22,23]. The actual cutoff is presumably higher, but very likely below the TeV region [24–26]. The cutoff frequency of PSR B1509–58 lies at about 10 MeV [27, 28]. As for the ms-pulsar PSR J0218+4232, there is circumstantial evidence for γ-rays up to 1 GeV [29,30].

The maximal energy of the source particles defined by $k_{\rm max}$ is much higher than the estimates in [2], which are in the low TeV range for the surface fields. In this reference, we considered electronic power-law averages and source counts dominated by the peaks of the spectral densities. Here, we focus on the fringes of the densities. The tachyonic spectral densities are much more extended than the electromagnetic synchrotron densities, where the exponential decay starts right at the spectral peak. In Fig. 1, the peak of the tachyonic synchrotron density is located at the tachyon mass, at 2 keV, whereas the critical frequency lies in the low GeV range. At lower Lorentz factors, the occasionally rather pronounced oscillations in the high-energy tails of the tachyonic densities, cf. Figs. 2–4, are absent in the electromagnetic counterpart, there is no photonic high-energy tail at all, just rapid decay after the spectral peak is reached. The high-energy tails of the tachy-

onic synchrotron densities suggest fringe particles cycling in the surface fields at energies reaching $k_{\max} = 12$, the 10^{21} eV region; cf. Table 5. These particles can be electrons as well as nuclei, since the critical frequency $\omega_{\rm ct}(E)$ is independent of the mass of the source particles, and so is the cutoff $E_{\max}$. If subjected to the voltage gap between the surface and light cylinder fields [31], they can spiral out of the magnetosphere as ultra-high-energy cosmic rays.

6 Conclusion

We have discussed tachyonic line spectra of hydrogenic ions and muonic atoms; cf. Sect. 3. The lines are very dim as compared to electromagnetic spontaneous emission, the line strength being weaker by about a factor of $\alpha_q/\alpha_e \approx 10^{-11}$ for the low-lying harmonics. The tachyonic quanta are partially longitudinally polarized, the lines are radiated in multiples of the gyrofrequency as listed in Table 1, clearly separated from the electromagnetic transition frequencies. Ionization cross-sections can be used to discriminate longitudinal tachyons from photons, as the transversal and longitudinal sections are peaked at different scattering angles [33, 34].

Continuum emission in the surface fields of γ-ray pulsars is discussed in Sect. 5. By equating the critical frequency with the observed spectral cutoff, we inferred the highest orbital energy attained in the surface fields. We concluded that γ-ray pulsars are a possible source of ultra-high-energy cosmic rays, capable of accelerating nuclei across the ankle of the cosmic ray spectrum into the 10^{21} eV region. As for extragalactic sources, tachyons do not interact with microwave and radio photons, so that there is no attenuation of tachyonic γ-rays.

We have here scrutinized very specific systems and a highly specialized radiation mechanism. We conclude by outlining the broader context, the general setup of tachyonic radiation theory, and contrast it with the electromagnetic counterpart, without going into any details, however. We will sketch the main features of the absorber theory mentioned in the Introduction, in particular the implied non-relativistic space conception.

In Sect. 2, we stated the tachyonic flux vectors generated by circularly orbiting charges, and we indicate here the basic steps in deriving them. The Lagrangian of the superluminal radiation field coupled to the subluminal source particle reads $L = L_{\rm tach} + L_{\rm elec}$, where

$$L_{\rm tach} = -\frac{1}{4}F_{\alpha\beta}F^{\alpha\beta} + \frac{1}{2}m_t^2 A_\alpha A^\alpha,$$
$$L_{\rm elec} = -m\sqrt{-\eta_{\alpha\beta}\dot{x}^\alpha\dot{x}^\beta} + qA_\alpha\dot{x}^\alpha. \qquad (6.1)$$

The sign conventions are $\eta_{\alpha\beta} = {\rm diag}(-1,1,1,1)$ and $m_t^2 > 0$. Estimates for the tachyon mass m_t and the tachyonic charge q, by which the tachyon field A_μ is minimally coupled to the electron, are given in Sect. 2, and $\hbar = c = 1$. We find the field equations, $(\Box + m_t^2)A_\mu = -j_\mu$ and $A^\mu{}_{,\mu} = 0$, where the sign convention for the d'Alembertian is $\Box = \eta^{\mu\nu}\partial_\mu\partial_\nu$. Wave solutions are obtained by applying the time symmetric Green function to the 4-current [5],

$$A^{\rm sym}_\mu(x) = \int G^{\rm sym}(x-x')j_\mu(x'){\rm d}x',$$
$$(\Box + m_t^2)G^{\rm sym}(t,\mathbf{x}) = -\delta(t)\delta(\mathbf{x}),$$
$$j^0 = q\delta(\mathbf{x}-\mathbf{x}(t)), \quad \mathbf{j} = q\mathbf{v}\delta(\mathbf{x}-\mathbf{x}(t)),$$
$$G^{\rm sym}(t,\mathbf{x}) \qquad (6.2)$$
$$= \frac{1}{4\pi}\delta(r^2-t^2) - \frac{m_t}{8\pi}\theta(r^2-t^2)\frac{J_1(m_t\sqrt{r^2-t^2})}{\sqrt{r^2-t^2}}.$$

There is no retarded or advanced Green function supported outside the lightcone, superluminal wave fields in a local Minkowskian setting are time symmetric and thus acausal. To break this symmetry, an external non-local absorber field is required.

Once the time symmetric field is calculated, the retarded and advanced components of $A^{\rm sym}_\mu = \frac{1}{2}(A^{\rm ret}_\mu + A^{\rm adv}_\mu)$ can be identified asymptotically, at large distance from the radiating source. The explicit knowledge of the asymptotic retarded radiation field suffices to calculate the line spectra and the spectral densities. The transversal and longitudinal flux vectors in Sect. 2 are found by substituting the asymptotic $A^{\rm ret}_\mu$ into the $T_0{}^n$ components of the energy-momentum tensor, $T_\mu{}^\nu = -F_{\lambda\mu}F^{\lambda\nu} + m_t^2 A_\mu A^\nu - \delta^\nu_\mu L_{\rm tach}$ [1].

The asymptotic $A^{\rm ret}_\mu$ can be extracted from the time symmetric solution $A^{\rm sym}_\mu$ of the wave equation, without reference to the cosmic absorber field. However, the retarded component is not a solution of the wave equation, there is no retarded Green function. This requires the existence of an external absorber, capable of turning the advanced component of the time symmetric field into the missing half of the retarded field, $A^{\rm ret}_\mu = A^{\rm sym}_\mu + A^{\rm abs}_\mu$.

The absorber field is generated by uniformly distributed microscopic oscillators of the cosmic absorber medium [35], via an instantaneous non-local interaction triggered by the advanced component of the time symmetric field. We do not need to know the details of this interaction, as we can extract the retarded field from the time symmetric solution of the wave equation, quite within the local Minkowskian framework. The rest frame of the absorber medium is the comoving galaxy frame, in which the oscillators have constant space coordinates.

When introducing a cosmic absorber medium as space structure, the most important thing is to keep it simple, to efficiently do physical modeling in it. Here, we have scrutinized the cyclotron and synchrotron mechanism, which is already in electrodynamics amongst the technically most difficult radiation problems, solved by systematic asymptotic summation of the multipole expansion. We have done this for the Proca field with negative mass square as well, but it is unlikely that we could have carried that through had we needed to explicitly take into account the microscopic space structure, the oscillators of the absorber medium. Instead, we invoke the absorber like the Mach principle is invoked in Newtonian mechanics, by its effect only. This principle asserts that the inertial force is

Table 7. Parameters determining the spectral densities of protons in the surface and light cylinder (lc) fields. The parameters listed in Tables 5 and 6 for electrons remain valid for protonic source particles, with the exception of the critical photon frequency $\omega_{\rm c}^{(p)}$, the tachyonic break energy $\hat{\omega}_{\rm b}^{(p)}$ (keV) $\approx 2.29\times 10^k$, and their ratio $\hat{\kappa}^{(p)} = \hat{\omega}_{\rm b}^{(p)}/\omega_{\rm c}^{(p)}$. The source energy is $E\,({\rm GeV}) = 10^k$, so that the scale factor v/c (orbital velocity) is now calculated with $\gamma \approx 1.066\times 10^k$; cf. the caption of Table 5. The lower limit on the source energy, $k_{\rm min}^{(p)} \approx -0.027$, is set by the proton mass, and the upper edge $k_{\rm max}$ is listed in Tables 5 and 6 for the surface and light cylinder fields, respectively

	$\omega_{\rm c}^{(p)}$ (keV)	$\hat{\kappa}^{(p)}$	$\omega_{\rm c}^{(p,{\rm lc})}$ (keV)	$\hat{\kappa}^{(p,{\rm lc})}$
γ-ray pulsars				
B1509–58	$1.66\times 10^{-1+2k}$	$1.38\times 10^{1-k}$	$4.54\times 10^{-10+2k}$	$5.05\times 10^{9-k}$
Crab	$4.06\times 10^{-2+2k}$	$5.64\times 10^{1-k}$	$1.05\times 10^{-8+2k}$	$2.17\times 10^{8-k}$
B1706–44	$3.35\times 10^{-2+2k}$	$6.83\times 10^{1-k}$	$2.92\times 10^{-10+2k}$	$7.84\times 10^{9-k}$
B1951+32	$5.22\times 10^{-3+2k}$	$4.39\times 10^{2-k}$	$7.93\times 10^{-10+2k}$	$2.89\times 10^{9-k}$
ms-pulsar				
J0218+4232	$4.61\times 10^{-6+2k}$	$4.97\times 10^{5-k}$	$3.45\times 10^{-9+2k}$	$6.64\times 10^{8-k}$

Table 8. Lorentz factors of cosmic rays originating as synchrotron electrons and protons in the surface and light cylinder fields. $\gamma^{(e,p)}(k_{\rm max})$ is the upper bound on the Lorentz factors of electrons/protons cycling in the surface fields, as determined by the $k_{\rm max}$-cutoffs listed in Table 5. In the surface fields, electrons as well as protons can reach energies in the 10^{19}–10^{21} eV region, above the ankle of the cosmic ray spectrum.The Lorentz factors $\gamma^{(e,p)}(k_{\rm max}^{(\rm lc)})$ refer to the much smaller cutoff energies $k_{\rm max}^{(\rm lc)}$ in the light cylinder fields; cf. Table 6

	$\gamma^{(e)}(k_{\rm max})$	$\gamma^{(e)}(k_{\rm max}^{(\rm lc)})$	$\gamma^{(p)}(k_{\rm max})$	$\gamma^{(p)}(k_{\rm max}^{(\rm lc)})$
γ-ray pulsars				
B1509–58	2.70×10^9	7.44	1.47×10^6	–
Crab	9.81×10^{13}	2.76×10^7	5.34×10^{10}	1.51×10^4
B1706–44	1.96×10^{15}	1.91×10^7	1.07×10^{12}	1.04×10^4
B1951+32	3.10×10^{14}	5.15×10^7	1.69×10^{11}	2.80×10^4
ms-pulsar				
J0218+4232	7.44×10^8	5.64×10^5	4.05×10^5	307

generated by some kind of instantaneous interaction with the cosmic matter distribution. However, when calculating trajectories in Newtonian mechanics, it is not necessary to know the details of this interaction, as the inertial force is known beforehand, even though it remains unexplained.

The local emission process is time symmetric, for every outgoing mode there is an identical incoming counterpart, retardation is achieved by superposition with the external absorber field. There is no radiation damping, the energy radiated is supplied by the absorber medium. (The incoming advanced field means energy gain, the outgoing retarded component energy loss. The net energy balance for $A_\mu^{\rm sym} = \frac{1}{2}(A_\mu^{\rm ret} + A_\mu^{\rm adv})$, the field generated by the source particle, is thus zero. The subtracted energy gain in $A_\mu^{\rm abs} = \frac{1}{2}(A_\mu^{\rm ret} - A_\mu^{\rm adv})$ means energy loss, so that $A_\mu^{\rm abs}$ carries the energy of $A_\mu^{\rm ret}$. No need to argue this in negative energies.) As in electrodynamics, we end up with retarded wave propagation, but the radiation mechanism outside the lightcone is quite different, as the retarded Green function is replaced by a time symmetric one, and we have to acknowledge the existence of the absorber field. The latter constitutes the fundamental difference between electromagnetic and superluminal wave propagation. The cosmic absorber destroys the seemingly close analogy (6.2) of electromagnetic and tachyonic wave propagation at an early stage, even though the retarded tachyonic wave fields can be calculated without knowledge of the absorber field (asymptotically at least, when positive and negative wave modes clearly emerge in $A_\mu^{\rm sym}$, otherwise we need to know the absorber field to find $A_\mu^{\rm ret}$). We exemplified the energy balance with superluminal cyclotron radiation. This radiation is not accompanied by atomic transitions, there is no energy transfer from the atom to the tachyons, as the energy radiated stems from the absorber. By contrast, if a tachyon is absorbed in an atomic transition [35], there is equal probability of reemission in the reverse transition

due to the symmetry of the Einstein coefficients, and there is no energy exchange with the absorber.

The absorber medium defines an absolute space, a universal frame of reference. We list some implications of this. There is the residual radiation in the limit of infinite gyroradius, cf. (4.28) and (4.29); charges in straight uniform motion in the absorber frame still radiate superluminal quanta, so that uniform motion and rest become distinguishable states [16]. The reference frame provided by the absorber medium is also necessary to define longitudinal and transversal wave modes, as Lorentz boosts mix them due to the spacelike wave vector [35]. Apart from advanced wave modes generated by the time symmetric Green function (which are cancelled by the absorber field), there is another even more generic source of causality violation arising in a relativistic spacetime conception. Lorentz boosts interchange the time order of spacelike connections, so that the time order of cause and effect is not preserved in different inertial frames. The rest frame of the absorber is once more required to define a universal cosmic time order of cause and effect to which every observer can relate [36].

The Lagrangians (6.1) are covariant, but the relativistic interpretation of Lorentz invariance is replaced by the absolute spacetime defined by the absorber [5, 37]. Proper account of this universal frame of reference must also be taken when quantizing superluminal wave fields, to obtain an unambiguous vacuum. Lorentz boosts mix positive and negative frequency modes (with spacelike wave vector), so that there is no relativistically invariant vacuum state. The cosmic absorber frame is needed to define a consistent occupation number representation [35]. The spin-statistics theorem is not applicable outside the light cone, and the classical energy functional ${T_0}^0$, cf. after (6.2), is indefinite. Once the longitudinal modes are identified in the absorber frame, they are quantized in Fermi–Dirac statistics to obtain a positive definite energy operator [33, 34]. Here, we have considered classical spectral densities; the quantization of tachyonic cyclotron and synchrotron radiation will be given elsewhere.

Acknowledgements. The author acknowledges the support of the Japan Society for the Promotion of Science. The hospitality and stimulating atmosphere of the Centre for Nonlinear Dynamics, Bharathidasan University, Trichy, and the Institute of Mathematical Sciences, Chennai, are likewise gratefully acknowledged.

References

1. R. Tomaschitz, Physica A **335**, 577 (2004)
2. R. Tomaschitz, Astropart. Phys. **23**, 117 (2005)
3. M. Nagano, A.A. Watson, Rev. Mod. Phys. **72**, 689 (2000)
4. J.A. Wheeler, R.P. Feynman, Rev. Mod. Phys. **17**, 157 (1945)
5. R. Tomaschitz, Class. Quantum Grav. **18**, 4395 (2001)
6. R. Tomaschitz, Eur. Phys. J. B **17**, 523 (2000)
7. J. Schwinger, Proc. Nat. Acad. Sci. **40**, 132 (1954)
8. J.J. Brainerd, V. Petrosian, Astrophys. J. **320**, 703 (1987); J.J. Brainerd, Astrophys. J. **320**, 714 (1987); J.N. Imamura, R.I. Epstein, V. Petrosian, Astrophys. J. **296**, 65 (1985)
9. V.L. Ginzburg, S.I. Syrovatskii, Ann. Rev. Astron. Astrophys. **3**, 297 (1965); **7**, 375 (1969)
10. R.I. Epstein, V. Petrosian, Astrophys. J. **183**, 611 (1973)
11. A.A. Sokolov, I.M. Ternov, Radiation from relativistic electrons (Hilger, Bristol 1986)
12. P.J. Mohr, G. Plunien, G. Soff, Phys. Rep. **293**, 227 (1998); M.I. Eides, H. Grotch, V.A. Shelyuto, Phys. Rep. **342**, 63 (2001)
13. E. Borie, G.A. Rinker, Rev. Mod. Phys. **54**, 67 (1982); D. Gotta, Prog. Part. Nucl. Phys. **52**, 133 (2004)
14. J.K. Tuli, Nuclear wallet cards, 7th ed. (Brookhaven Nat. Lab., Upton, NY, 2005), http://www.nndc.bnl.gov/wallet/
15. G.N. Watson, A treatise on the theory of Bessel functions (Cambridge Univ. Press, Cambridge, 1996)
16. R. Tomaschitz, Physica A **320**, 329 (2003)
17. V. Petrosian, Astrophys. J. **251**, 727 (1981); K.-L. Klein, Astron. Astrophys. **183**, 341 (1987)
18. G.A. Schott, Electromagnetic radiation (Cambridge Univ. Press, Cambridge, 1912)
19. M. Abramowitz, I.A. Stegun, Handbook of mathematical functions (Nat. Bureau of Standards, Washington DC, 1972)
20. J. Schwinger, Phys. Rev. **75**, 1912 (1949)
21. J.M. Fierro et al., Astrophys. J. **494**, 734 (1998)
22. D.J. Thompson et al., Astrophys. J. **465**, 385 (1996)
23. P.V. Ramanamurthy et al., Astrophys. J. **447**, L109 (1995)
24. T. Kifune et al., Astrophys. J. **438**, L91 (1995)
25. R. Srinivasan et al., Astrophys. J. **489**, 170 (1997)
26. F. Aharonian et al., Astrophys. J. **614**, 897 (2004)
27. L. Kuiper et al., Astron. Astrophys. **351**, 119 (1999)
28. T. Sako et al., Astrophys. J. **537**, 422 (2000)
29. L. Kuiper et al., Astrophys. J. **577**, 917 (2002)
30. L. Kuiper, W. Hermsen, B. Stappers, Adv. Space Res. **33**, 507 (2004)
31. K.S. Cheng, C. Ho, M. Ruderman, Astrophys. J. **300**, 500 (1986)
32. R.N. Manchester et al., Astron. J. **129**, 1993 (2005), http://www.atnf.csiro.au/research/pulsar/psrcat/
33. R. Tomaschitz, Eur. Phys. J. D **32**, 241 (2005)
34. R. Tomaschitz, J. Phys. A **38**, 2201 (2005)
35. R. Tomaschitz, Physica A **293**, 247 (2001); **307**, 375 (2002)
36. R. Tomaschitz, Celest. Mech. Dyn. Astron. **77**, 107 (2000)
37. R. Tomaschitz, Chaos Solitons Fractals **7**, 753 (1996); **20**, 713 (2004)